J. Fluid Mech. (2024), *vol.* 997, A49, doi:10.1017/jfm.2024.663

Bouncing behaviour of a particle settling through a density transition layer

Shuhong Wang[1,2], **Prabal Kandel**[1,2], **Jian Deng**[1,†], **C.P. Caulfield**[3]
and Stuart B. Dalziel[3]

[1]State Key Laboratory of Fluid Power and Mechatronic Systems, Department of Mechanics,
Zhejiang University, Hangzhou 310027, PR China

[2]Huanjiang Laboratory, Zhuji 311816, PR China

[3]Department of Applied Mathematics and Theoretical Physics, University of Cambridge,
Cambridge CB3 0WA, UK

(Received 10 October 2023; revised 11 July 2024; accepted 30 July 2024)

The present work focuses on a specific bouncing behaviour as a spherical particle settles through a density interface in the absence of a neutral buoyant position. This behaviour was initially discovered by Abaid *et al.* (*Phys. Fluids*, vol. 16, issue 5, 2004, pp. 1567–1580) in salinity-induced stratification. Both experimental and numerical investigations are conducted to understand this phenomenon. In our experiments, we employ particle image velocimetry (PIV) to measure the velocity distribution around the particle and to capture the transient wake structure. Our findings reveal that the bouncing process begins after the wake detaches from the particle. The PIV results indicate that an upward jet forms at the central axis behind the particle following wake detachment. By performing a force decomposition procedure, we quantify the contributions from the buoyancy of the wake (F_{sb}) and the flow structure (F_{sj}) to the enhanced drag. It is observed that F_{sb} contributes primarily to the enhanced drag at the early stage, whereas F_{sj} plays a critical role in reversing the particle's motion. Furthermore, our results indicate that the jet is a necessary condition for the occurrence of the bouncing motion. We also explore the minimum velocities (where negative values denote the occurrence of bouncing) of the particle, while varying the lower Reynolds number Re_l, the Froude number Fr, and the upper Reynolds number Re_u, within the ranges $1 \leqslant Re_l \leqslant 125$, $115 \leqslant Re_u \leqslant 356$ and $2 \leqslant Fr \leqslant 7$. Our findings suggest that the bouncing behaviour is influenced primarily by Re_l. Specifically, we observe that the bouncing motion occurs below a critical lower Reynolds number $Re_l^* = 30$ in our experiments. In the numerical simulations, the highest value for this critical number is $Re_l^* = 46.2$, which is limited to the parametric ranges studied in this work.

Key words: stratified flows, particle/fluid flow

---

† Email address for correspondence: zjudengjian@zju.edu.cn

1. Introduction

Density stratification resulting from non-uniform temperature or salinity distributions is prevalent in oceans and lakes. Such stratification affects the settling or rising of submerging particles, and has significant impacts on environmental issues such as marine snow aggregation, thin layer formation, oil spill dispersion and sediment deposition (Prairie & White 2017; Diercks *et al.* 2019). Therefore, comprehending the fluid dynamics of particle settling (or rising) in a stratified ambient fluid is crucial for accurate predictions of such actions.

In a homogeneous fluid, the hydrodynamic force acting on a particle accelerating under gravity can be decomposed into buoyancy force, steady drag, added mass and history (Basset) force. The steady drag increases with velocity and ultimately balances the reduced gravity, resulting in a steady particle velocity. However, in a stratified fluid, the particle experiences an additional drag force caused by the stratification, referred to as 'stratification drag'. As a result, the settling velocity of particles in a stratified fluid is significantly reduced (Srdić-Mitrović, Mohamed & Fernando 1999; Abaid *et al.* 2004; Camassa *et al.* 2009; Yick *et al.* 2009; Camassa *et al.* 2010; Doostmohammadi, Dabiri & Ardekani 2014*b*; Verso, van Reeuwijk & Liberzon 2019; Magnaudet & Mercier 2020; Mandel *et al.* 2020).

There exist various explanations for the origin of stratification drag. Among these, the widely accepted one is that it arises due to the buoyancy of the associated lighter upper fluid, as the settling particle distorts the isopycnals, leading to the dragging of some upper fluid to a lower position. This phenomenon is commonly referred to as the entrainment of the lighter fluid, and the volume of fluid carried along is termed drift or partial drift volume (Magnaudet & Mercier 2020; More & Ardekani 2023). In an attempt to understand this phenomenon, Srdić-Mitrović *et al.* (1999) carried out experiments in which particles were made to settle in a three-layer stratified fluid consisting of two homogeneous layers and a density transition layer (interface) in between, at Reynolds numbers $1.5 \leqslant Re \leqslant 15$ and Froude numbers $3 \leqslant Fr \leqslant 10$. They observed that the total drag enhancement could be estimated by considering the total buoyancy of the upper fluid dragged below the upper bound of the interface, before the maximum drag was reached. They also noted that the contribution of internal waves was negligible before the wake breaks, as these waves were generated only after the rupture of the wake. Verso *et al.* (2019) conducted experiments with four different particles, settling in the same type of stratification, but in a wider parameter range ($2 \leqslant Re \leqslant 106$ and $0.5 \leqslant Fr \leqslant 28$). They developed a time-dependent stratification force model for these particles, which assumed that the stratification force was entirely contributed by the buoyancy of an effective wake. The wake volume was assumed to be constant within the interface and decrease exponentially until a new terminal velocity was reached.

In the study by Yick *et al.* (2009), a combined experimental and numerical investigation study focused on settling particles in a linearly stratified fluid at small Reynolds numbers ($Re \sim O(1)$). They found that the buoyancy of a shell of fluid around the particle, rather than the entire distorted region, is responsible for the drag enhancement. Moreover, they proposed that the total drag increment can be scaled by a dimensionless parameter, the Richardson number, which delineates the relative significance of buoyancy and viscous shear forces. A similar mechanism was found for the stratification drag experienced by a rising grid of bars by Higginson, Dalziel & Linden (2003), albeit at significantly higher Reynolds numbers ($Re \sim O(10^3)$). They approximated the volume of dragged fluid using the drift volume in inviscid fluid, showcasing a comparable trend.

While buoyancy explains the stratification drag in numerous instances, Torres *et al.* (2000) was the first to propose that the augmented drag arises from the specific flow structure. They found that the drag enhancement remains minimal until a vertical upward jet forms at the rear of the particle, particularly under strong stratification conditions ($Fr \lesssim 20$). Utilising Bernoulli's theorem, they elucidated the generation of this 'jet', and suggested that the associated low-pressure zone behind the particle is responsible for the enhanced drag. More recently, Zhang, Mercier & Magnaudet (2019) employed a force decomposition technique to quantify the drag force arising from various mechanisms. Their findings indicated that the vorticity field induced by buoyancy effects contributes predominantly to the stratification drag, with buoyancy itself playing a secondary role. They also proposed scaling laws for different stratification drag components based on theoretical analysis. Several of their predictions have since been confirmed in subsequent experiments and numerical simulations (Mandel *et al.* 2020; Ahmerkamp *et al.* 2022).

The flow structure exhibited by the vertical motion of a particle in a stratified fluid is significantly different to that in a homogeneous fluid. In a stratified fluid, the baroclinic torque ($\nabla\rho \times \nabla p$) results in vorticity generation whenever there is a misalignment between density and pressure gradient (Magnaudet & Mercier 2020). For low Reynolds numbers ($Re \ll 1$), top-down symmetrical toroidal eddies are induced by a vertical, downward point force (Stokeslet) under linear stratification, which is similar to the eddy formed under the restriction of two horizontal walls, indicating the suppression of vertical flow by stratification (Ardekani & Stocker 2010). For higher Reynolds numbers ($0.05 \leqslant Re \leq 100$), toroidal eddies still exist but lose the top-down symmetry, and a vertical upward jet is simultaneously generated at the centreline downstream of the particle (Zhang *et al.* 2019). This jet was observed experimentally over a wide range of Froude numbers ($0.1 \leqslant Fr \leqslant 35$) and Reynolds numbers ($30 \leqslant Re \leqslant 4000$), with its shape and strength varying with Re and Fr (Hanazaki, Kashimoto & Okamura 2009).

The intricate fluid dynamics that arises from particle interactions in stratified fluids results in several counter-intuitive behaviours. For instance, the settling velocity of a particle varies non-monotonically as it passes through a density interface or settles in linear stratification (Srdić-Mitrović *et al.* 1999; Doostmohammadi *et al.* 2014*b*; Verso *et al.* 2019). Remarkably, a particle can sometimes experience a negative velocity during sedimentation as it traverses an interface with a large density gradient, despite having a density that is always higher than the fluid, and no neutral position exists (Abaid *et al.* 2004). In this scenario, the particle experiences substantial stratification drag, exceeding the reduced gravity and leading to a reversal in particle motion. Yet while steady or quasi-steady drag has been examined extensively, only a limited number of studies have delved into the transient stratification drag accompanying this bouncing behaviour.

The discoverers of this phenomenon, Abaid *et al.* (2004), observed in their experiments that a plume forms in the near-wake of the particle and ascends to the top layer before the particle reverses its motion. They proposed that the ascending plume is responsible for the bouncing motion. More recently, Camassa *et al.* (2008) and Verso *et al.* (2019) suggested that the bouncing motion occurs only when the combined buoyancy of the drift fluid and particle exceeds the gravitational force acting on the particle, assuming that the enhanced drag is entirely due to the enhanced buoyancy of the drift fluid. These studies propose different drag enhancement mechanisms, and no consensus has been reached yet.

This study aims to offer more in-depth insights into the phenomena of stratification drag and the mechanisms governing bouncing motion. To our knowledge, Abaid *et al.* (2004) is the sole experimental investigation that has captured bouncing behaviour using shadowgraph techniques. With the advancement of experimental equipment and techniques, it has become feasible to conduct comprehensive whole-field density and velocity measurements in stratified fluids. For instance, in studies involving a particle moving stably in linearly stratified fluid, researchers such as Hanazaki *et al.* (2009) and Okino, Akiyama & Hanazaki (2017) employed particle image velocimetry (PIV) to assess the velocity distribution around the particle and within the jet. Additionally, Okino *et al.* (2021) utilised laser-induced fluorescence to measure the density distribution surrounding the particle, including within the thin density boundary layer and the jet. However, experimental measurements of the velocity and density distribution during the transient process of freely settling particles have yet to be conducted. Such measurements are crucial for gaining a comprehensive understanding of the bouncing mechanism. For simplification purposes, this study focuses solely on spherical particles and disregards particle rotation. Investigations involving non-spherical particles settling through a density interface can be found in Doostmohammadi & Ardekani (2014*a*), Mrokowska (2018, 2020) and More *et al.* (2021).

Before delving into the mechanisms of bouncing, a parametric study is conducted to identify the parameter regime in which bouncing occurs. Previous research has demonstrated that the bouncing behaviour is influenced by various parameters. For instance, Camassa *et al.* (2022) discovered that the critical particle density ρ_p for bouncing can be expressed as a linear combination of the densities of the upper and lower fluid layers. Moreover, Doostmohammadi & Ardekani (2014*a*) observed that at a relatively higher density ratio $(\rho_l - \rho_u)/\rho_u$, an ellipsoid could bounce briefly as it traverses a density interface. Additionally, Blanchette & Shapiro (2012) discovered that a high ratio $(\rho_p - \rho_u)/(\rho_p - \rho_l)$ could cause a drop to undergo temporary reverse motion as it descends through a density transition layer with the same surface tension. Furthermore, the Froude number is a crucial parameter affecting the oscillation of a particle or droplet near its neutral buoyancy point in a linearly stratified fluid (Bayareh *et al.* 2013; Doostmohammadi *et al.* 2014*b*). In the experiments conducted by Abaid *et al.* (2004), the transient levitation of particles was discovered by decreasing the lower terminal velocities, indicating that the lower Reynolds number should be considered.

The aforementioned studies suggest that the bouncing behaviour is influenced by various parameters, including the ratio of densities, the ratio of density differences, Froude number and Reynolds number. However, some of these parameters are correlated, necessitating the selection of the smallest set of parameters controlling the bouncing motion.

For a particle in a three-layer stratified fluid, the terminal velocities in the upper and lower layers are determined by the force balance

$$F_d = G - F_b, \tag{1.1}$$

where F_d is the steady drag, G is gravity, and F_b is the buoyancy force. Here, F_d is defined as

$$F_d = \tfrac{1}{2} C_d(Re) \rho_f U_f^2 S_p, \tag{1.2}$$

where C_d is the drag coefficient depending solely on Re, S_p is the cross-sectional area of the particle, ρ_f and U_f refer to the density and terminal velocity in the upper or lower fluid. Equation (1.1) leads to a relation between the terminal velocity and the densities:

$$\tfrac{1}{2} C_d(Re)\, \rho_f U_f^2 S_p = (\rho_p - \rho_f) g V_p, \tag{1.3}$$

where ρ_p is the particle density, and V_p is the particle volume. Then the terminal velocity is determined by

$$U_f = \sqrt{\frac{\rho_p - \rho_f}{\rho_f} \frac{4gD}{3C_d(Re)}}. \tag{1.4}$$

Parameter	Symbol	Definition	Range of values
Particle density	ρ_p	—	1121.58–1125.26 kg m^{-3}
Particle diameter	D	—	10.055–10.128 mm
Particle velocity	U	—	−0.559–4.908 cm s^{-1}
Jet velocity	u_j	—	—
Upper fluid density	ρ_u	—	1113.92–1118.63 kg m^{-3}
Lower fluid density	ρ_l	—	1121.45–1123.66 kg m^{-3}
Interface thickness	L	—	2.52–13.06 cm
Upper Reynolds number	Re_u	$\rho_u U_u D/\mu_u$	115–356
Lower Reynolds number	Re_l	$\rho_l U_l D/\mu_l$	1–125
Froude number	Fr	U_u/ND	2–7
Brunt–Väisälä frequency	N	$\sqrt{(g(\rho_l-\rho_u)/L\rho_{ref})}$	0.62–1.88
Reference density	ρ_{ref}	$(\rho_u+\rho_l)/2$	1118.08–1120.09 kg m^{-3}
Prandtl number	Pr	ν/κ	~ 700
Density ratio	$\Delta\rho_l$	$(\rho_p-\rho_l)/\rho_l$	$(0.03\text{–}2.54)\times 10^{-3}$

Table 1. Definitions and ranges of parameters covered in the present work.

Therefore, the influences of the upper and lower density ratios, $\Delta\rho_u = (\rho_p - \rho_u)/\rho_u$ and $\Delta\rho_l = (\rho_p - \rho_l)/\rho_l$, are included in the upper and lower Reynolds numbers (defined as $Re_u = U_u D/\nu_u$ and $Re_u = U_u D/\nu_u$, respectively) through the terminal velocities U_u and U_l.

Another feature of stratified fluid is the density gradient, which can be characterised by the Froude number, defined as $Fr = U_u/ND$, where N is the Brunt–Väisälä frequency, representing the natural oscillation frequency of a vertically displaced parcel in a stratified fluid, calculated as

$$N = \sqrt{\frac{g}{\rho_{ref}}\frac{\rho_l - \rho_u}{L}}, \tag{1.5}$$

where L is the thickness of the density transition layer.

In the current study, the problem is characterised using Re_u, Re_l and Fr. A systematic study is conducted over parameter ranges $1 \leqslant Re_l \leqslant 125$, $115 \leqslant Re_u \leqslant 356$ and $2 \leqslant Fr \leqslant 7$. All relevant parameters are listed in table 1.

The paper is structured as follows. Section 2 introduces the experimental methodology, comprising the experimental set-up and measurement techniques. The numerical methodology and validation process are presented in § 3. Section 4 discusses the results, starting with the transient flow structure and force analysis during the settling process to gain insights into the bouncing mechanisms. Next, the effects of the Reynolds number of the lower layer, Froude number, and Reynolds number of the upper layer on the minimal velocity of the particle are examined to identify the primary controlling parameter. Finally, § 5 presents the conclusions of the study.

2. Experimental approach

2.1. *Experimental set-up*

The experiments were conducted in an experimental tank made of glass, with total depth 60 cm to ensure that terminal velocity was achieved. To avoid interaction between the particle and the tank walls, the tank has a large base area, 30 cm × 30 cm. The working fluids are prepared by dissolving salt in fresh water, with different concentration ratios in

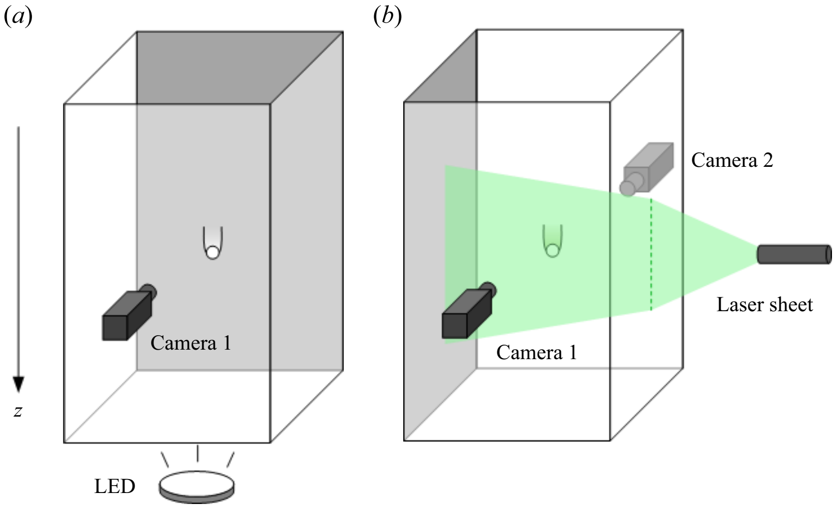

Figure 1. Experimental set-ups: (*a*) set-up 1 for recording particle trajectories; (*b*) set-up 2 for simultaneous wake visualisation and PIV measurement.

separate buckets. The solution is kept at room temperature for at least 24 h before filling the tank, to eliminate resolved gas and achieve a uniformly stable concentration distribution.

Initially, the tank is half-filled with heavy fluid. Then the light fluid is pumped slowly and horizontally to the top of the heavy fluid using a micro pump, at a low flow rate 100 ml $\min^{-1}$, to minimise mixing of the two fluids. This filling method results in an error-function-type density profile. The tank is allowed to stand for at least half an hour after filling, and before the experiments, to reduce disturbances caused by the pumping. The standing time varies with cases to achieve different thicknesses of the transition layer; a thicker transition layer requires longer time for the interdiffusion of two fluids.

Spherical non-porous and reusable nylon particles with diameter $D \sim 10$ mm and densities ranging from 1120 to 1130 kg cm^{-3} are used in the experiments. Before each experiment, the particles are fixed at the centre of the experimental tank cross-section, 15 cm from the side walls, 2 cm below the free surface, and approximately 25 cm above the density transition layer. Subsequently, the clamp is opened cautiously to release the particle without disturbing the fluid. The time interval between each release is approximately 10 min, ensuring that the fluid is relaxed to its quiescent state. The settling process of the particles is captured by a high-speed camera at frame rate 100 fps.

Two distinct experimental set-ups are employed, as depicted in figure 1, to meet the requirements for capturing particle trajectories and measuring surrounding flow fields, respectively. To record the particle trajectories, a single camera is positioned on one side of the tank, with bottom illumination provided by a panel of light-emitting diodes (LEDs) (see figure 1*a*). The opposite sidewall of the tank is coated with black paint to prevent light reflection. Except for PIV measurements, the camera captures a window approximately $20 \times 20\ \mathrm{cm}^2$ in size, with 1024×1024 pixels, yielding resolution 0.2 $\mathrm{mm pixel}^{-1}$. The PIV experiments utilise a closer view of $9.4 \times 7.3\ \mathrm{cm}^2$, with higher image resolution 2048×1600 pixels, resulting in a finer resolution 4.6×10^{-5} mm pixel^{-1}.

In the second experimental set-up, Rhodamine B dye is used to visualise the upper fluid, while seeding particles are added to both the upper- and lower-layer fluids for PIV measurements. To simultaneously capture the visualised wake structure and measure the velocity fields, two cameras are positioned at opposite sides of the tank and carefully aligned to ensure that their optical axes are parallel (as illustrated in figure 1*b*). The centre plane of the tank perpendicular to the camera optical axis is illuminated by a 2 mm thick laser sheet from the side. The two cameras are synchronised to obtain simultaneous image pairs, with one camera equipped with a long-pass filter to capture the dyed wake, and the other with a short-pass filter to obtain images of seeding particles. To capture the flow structure of the entire settling process, it is crucial that the particle remains within the illuminated laser sheet plane. Therefore, the densities of the particle and fluid must be selected carefully to prevent any out-of-plane motion, and the particle must be released with great care to minimise disturbances. It is worth mentioning that the laser sheet heats the fluid near the particle surface, which has a negligible effect in the upper layer, as the vicinity fluid circulates with the surrounding fluid and transfers the heat away quickly. However, as the particle bounces and is retained at the interface, the heated fluid at the particle surface becomes lighter and rises, which increases the drag acting on the particle and prolongs the particle's suspending time at the interface. Nevertheless, for flow visualisation and PIV measurements, where the focus is on the flow structure and velocity distribution, the laser sheet is still an effective illumination approach.

2.2. *Experimental measurements*

To measure the density distribution of the transition layer, 12 thin needles are inserted horizontally into the tank from punched holes at the sidewall, with 4 mm vertical intervals, and connected to 12 syringes for taking samples. Each sample takes 2.5 ml fluid, and a total of 30 ml fluid is taken for each measurement, leading to a variation in height of less than 0.4 mm. Thus the modification to the density distribution is negligible. These samples are then measured using a density meter (Anton-Parr DMA 4500) with accuracy 0.01 kg m^{-3}. Density distribution measurements are performed twice for each test, before and after dropping the particles. The measured density of the 12 samples is fitted to an error-function-shaped function, given by

$$\rho = \frac{\rho_u + \rho_l}{2} + \frac{\rho_u - \rho_l}{2} \operatorname{erf}(\alpha(z - z_{ref})), \tag{2.1}$$

which satisfies the density distribution in the transition layer. The parameters ρ_u and ρ_l are the upper- and lower-layer fluid densities, z_{ref} is the reference height, corresponding to the centre of the density transition layer, α is a scaling factor determining the thickness of the density transition layer, and $\operatorname{erf}(x)$ is the error function, which is written as

$$\operatorname{erf}(x) = \frac{2}{\pi} \int_0^x \mathrm{e}^{-t^2}\, \mathrm{d}t. \tag{2.2}$$

The measured density profiles for one of the experiments are presented in figure 2(*a*). The density profile becomes smoother after the experiment. We take the region covering 98 % of the density variation as the density interface thickness. The average of these two measurements is used as the final interface thickness, represented by the shaded area in figure 2(*a*).

It is crucial to monitor and control the temperature during experiments due to its impact on fluid and particle densities. For instance, with salinity 16 % and temperature 18 °C (for the current working fluid), a temperature variation 1 °C can lead to a density variation 0.41 kg m^{-3} for the fluid. Likewise, due to manufacturing discrepancies, particles respond

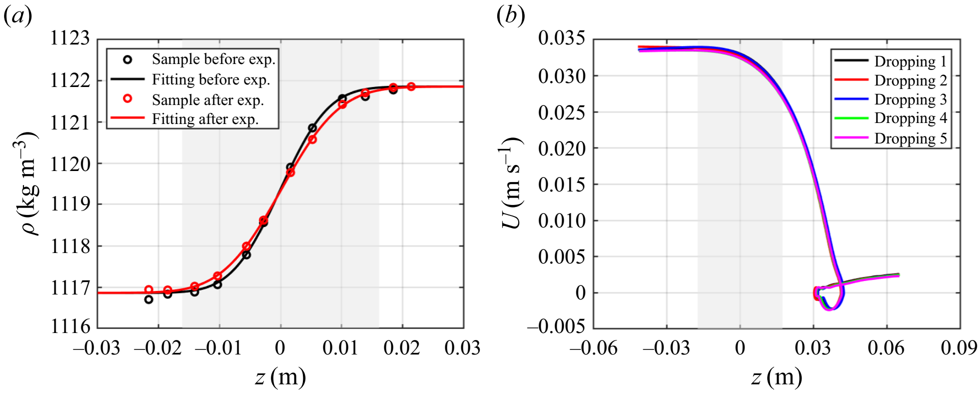

Figure 2. (*a*) Density distribution before and after the experiments. The grey area represents the density interface, which covers 98 % of density variation between the upper and lower layers. (*b*) Velocity profiles of five repeated droppings of the same particle.

differently to temperature changes. In our experiments, a temperature fluctuation 1 °C results in a density variation ranging from 0.35 to 0.45 kg m^{-3} for the particles.

Given the sensitivity of the bouncing motion to density differences between the lower-layer fluid and the particle, even a slight increase in density difference of 0.1 kg m^{-3} can significantly alter settling behaviour, potentially transitioning from bouncing to unidirectional settling. It is worth noting that reproducing the bouncing behaviour is challenging, even with the same particle and the same upper and lower fluids, without accounting for temperature effects.

To mitigate temperature variations in the working fluid, experiments are conducted in an enclosed room with the temperature controlled by an air conditioner. Real-time temperature monitoring ensures that temperature variations remain below 1 °C for all tests. To minimise the temperature influences on particle densities, particles are stored in a water tank (storing tank) where temperature fluctuations are less pronounced compared to the air. The storing tank, with dimensions 50 cm height and 10 cm × 10 cm cross-section, is filled with continuous stratified salty water prepared using the double-bucket method (Economidou & Hunt 2009). The stratified fluid in the storing tank allows for accurate measurement of particle densities. Particle density is determined by measuring the fluid density at the height of the particle centre, ensuring comparable accuracy with the fluid density.

Individual density measurements for particles are conducted before release. For each particle, three syringes of fluid samples (2.5 ml each) are taken at the height of the particle centre, and the average density of these samples is recorded as the particle density. After measurements, particles are taken out from the storing tank and clamped in the experimental tank, and their diameter is measured post-experimentation using a micrometer with accuracy 0.001 mm.

The viscosity of the fluid is calculated using an empirical formula with accuracy ±1.5 %, described in (22) of Sharqawy, Lienhard & Zubair (2010):

$$\left\{\begin{array}{l}\mu = \mu_w(1 + a_1 S_a + a_2 S_a^2),\\ \mu_w = 4.2844 \times 10^{-5} + (0.157(T_e + 64.993)^2 - 91.296)^{-1},\\ a_1 = 1.541 + 1.998 \times 10^{-2} T_e - 9.52 \times 10^{-5} T_e^2,\\ a_2 = 7.974 - 7.561 \times 10^{-2} T_e + 4.724 \times 10^{-4} T_e^2.\end{array}\right. \tag{2.3}$$

The formula consists of two equations. The first equation calculates the viscosity μ as a function of the salinity S_a and two constants, a_1 and a_2. The second equation calculates μ_w, a constant used in the first equation. The values of a_1, a_2 and μ_w are determined based on the temperature T_e.

Instantaneous particle displacements are obtained by fitting the discrete time-dependent position points with a quantic smoothing spline, following the methods of Truscott, Epps & Techet (2012) and Epps (2010). A fitting error tolerance $E = 1 \times 10^{-7}\ \mathrm{m}^2\ \mathrm{s}^{-1}$ is used for all experimental position data, which provides accurate fitting data and smooth fitting derivatives. The velocity and acceleration of the particles are then calculated based on the time histories of the fitted particle displacements.

Because the passing of particles introduces disturbances to the density transition layer and expedites the diffusion, no more than five particles are dropped in each fluid tank. Before the experiment, repeatability validation is conducted separately. The settling velocities are almost unchanged for the repeated releases, as shown in figure 2(*b*).

3. Numerical method

3.1. *Numerical model*

We solve the time-dependent incompressible Navier–Stokes equations with the finite volume method (Ferziger & Perić 2002). The momentum equation is solved on a moving grid domain using the arbitrary Lagrangian Eulerian formulation (Jasak 2009). The same framework of dynamic mesh has also been adopted in our previous study in a homogeneous flow (Deng & Caulfield 2016).

The integral form of the governing (conservation) equation in an arbitrary moving volume V bounded by a closed surface S is

$$\frac{\partial}{\partial t}\int_V \rho \boldsymbol{u}\,\mathrm{d}V + \oint_S \mathrm{d}\boldsymbol{s}\boldsymbol{\cdot}\rho(\boldsymbol{u}-\boldsymbol{u}_b)\boldsymbol{u} = \oint_S \mathrm{d}\boldsymbol{s}\boldsymbol{\cdot}(-p\boldsymbol{I} + \mu\,\boldsymbol{\nabla}\boldsymbol{u}) + \int_V \rho\boldsymbol{g}\,\mathrm{d}V, \tag{3.1}$$

where ρ is the fluid density, $\boldsymbol{u}$ is the fluid velocity, $\boldsymbol{u}_b$ is the boundary velocity of a control volume, and p is the pressure. The Boussinesq approximation is applied to account for the stratification effect, where the density variation enters the momentum equation only through the buoyancy term. Division by the reference density in (3.1) yields

$$\frac{\partial}{\partial t}\int_V \boldsymbol{u}\,\mathrm{d}V + \oint_S \mathrm{d}\boldsymbol{s}\boldsymbol{\cdot}(\boldsymbol{u}-\boldsymbol{u}_b)\boldsymbol{u} = \oint_S \mathrm{d}\boldsymbol{s}\boldsymbol{\cdot}\left(-\frac{p}{\rho_{ref}}\boldsymbol{I} + \nu\,\boldsymbol{\nabla}\boldsymbol{u}\right) + \int_V \frac{\rho}{\rho_{ref}}\boldsymbol{g}\,\mathrm{d}V, \tag{3.2}$$

with kinematic viscosity $\nu = \mu/\rho_{ref}$. The transport equation for density is given as

$$\frac{\partial}{\partial t}\int_V \rho\,\mathrm{d}V + \oint_S \mathrm{d}\boldsymbol{s}\boldsymbol{\cdot}\rho(\boldsymbol{u}-\boldsymbol{u}_b) = \oint_S \mathrm{d}\boldsymbol{s}\boldsymbol{\cdot}(\kappa\boldsymbol{\nabla}\rho), \tag{3.3}$$

where κ is the scalar diffusivity, defined as $\kappa = \nu/Pr$. In our simulations, we choose Prandtl number $Pr = 700$, corresponding to the salinity-induced stratification in water.

The present study focuses on moderate Reynolds numbers ($Re \leq 356$), where the axisymmetric assumption can be applied. Previous numerical investigations by Doostmohammadi *et al.* (2014*b*) observed that the flow remains axisymmetric up to Reynolds number 353 without vortex shedding when a particle settles in a linearly stratified fluid. Additionally, Torres *et al.* (2000) demonstrated the maintenance of a nearly axisymmetric structure at $Re \sim 800$ for a uniformly moving particle (Torres *et al.* 2000; Doostmohammadi *et al.* 2014*b*).

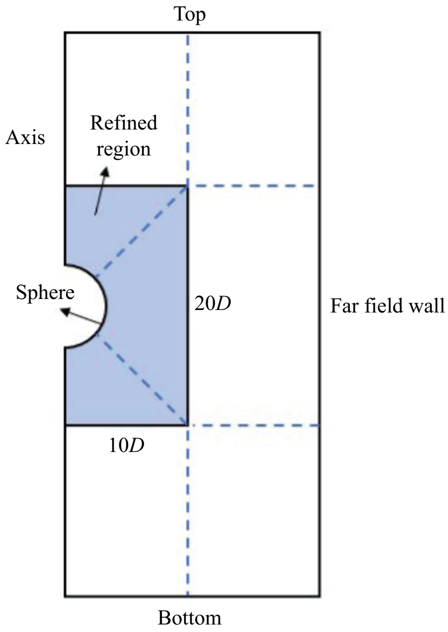

Figure 3. Illustration of the computational domain. The blue dashed lines show the boundaries of blocks for mesh generation.

For spatial discretisation, second-order upwind schemes are employed for the convection terms, and central differences are used for the Laplacian terms. The time discretisation follows a second-order implicit Euler method. The PISO (pressure-implicit with splitting of operators) scheme is employed for the pressure–velocity coupling. The computational domain is illustrated in figure 3.

The domain size is $25D \times 90D$. For mesh generation, the whole domain is divided into 8 blocks (as depicted by the blue dashed lines in figure 3). An O-grid is used around the sphere within a region of size $10D \times 20D$, which is denoted as the refined region. In this region, the grid size increases exponentially with a fixed rate from the particle surface ($0.0014D$) to its boundary ($0.0975D$). Rectangular cells with constant spacing are used outside the refined region.

The motion of the sphere is achieved using a whole domain moving strategy. For each time step, the total hydro-force F_{hydro} acting on the particle is calculated as

$$F_{hydro} = -\int_S p\boldsymbol{n}\,\mathrm{d}S - \int_S \mu(\nabla\boldsymbol{u} + \nabla\boldsymbol{u}^{\mathrm{T}}) \cdot \boldsymbol{n}\,\mathrm{d}S, \tag{3.4}$$

where $\boldsymbol{n}$ represents the unit normal to the surface pointing outside. The total force is then calculated as $F_t = G + F_{hydro}$. The motion of the particle is governed by the equation

$$\rho_p \frac{1}{6}\pi D^3 \frac{\mathrm{d}^2 z}{\mathrm{d}t^2} = F_t. \tag{3.5}$$

The boundary conditions are set as follows. For velocity, a no-slip boundary condition for moving mesh ($\boldsymbol{u} = \boldsymbol{u}_b$) is imposed on the sphere surface, while a zero-gradient (normal gradient at the patch is zero) condition is applied to all other boundaries. For pressure ($p_{rgh} = p - \rho\boldsymbol{g} \cdot \boldsymbol{h}$), a fixed value of zero is imposed on the top boundary, and a fixed-flux

Mesh no.	First-layer thickness	Maximum grid size	Total cell number
1	$0.0056D$	$0.3847D$	23 425
2	$0.0037D$	$0.2566D$	52 539
3	$0.0028D$	$0.1943D$	93 050
4	$0.0019D$	$0.1296D$	209 850
5	$0.0014D$	$0.0975D$	348 000

Table 2. Detailed information for five different mesh resolutions used for the resolution tests.

condition is adopted for the pressure at all other boundaries, which sets the pressure gradient to the provided value such that the flux on the boundary is that specified by the velocity boundary condition. For density, fixed values are imposed on the top and bottom boundaries (ρ_u and ρ_l, respectively), while a zero-gradient condition ($\boldsymbol{n} \boldsymbol{\cdot} \nabla \rho = 0$) is applied to other boundaries.

In each simulation, the particle is allowed to settle for 10 s in the upper-layer fluid to ensure that it has reached a steady velocity. The simulation ends 80 s after the particle enters the interface. Each case takes 2 days to complete, running on 16 AMD cores.

3.2. *Numerical validation*

Initially, we conduct a mesh resolution test to assess the performance of five different meshes. The domain size is fixed at $25D \times 90D$, and a consistent refinement strategy is applied across all testing meshes, as illustrated in figure 3. The five testing meshes differ in their first-layer thickness (of the particle surface), each with a fixed growth rate, resulting in varying maximum grid sizes and total cell numbers. These specifications are detailed in table 2.

The settling velocities of the particle simulated on the testing meshes are depicted in figure 4, considering a particle settling in a three-layer stratified fluid with $Re_u = 198$, $Re_l = 26$ and $Fr = 2.3$. Notably, the results exhibit strong convergence for meshes 4 and 5.

Furthermore, we compare the density and velocity fields along the central axis near the lower surface of the particle for different meshes in figure 5. The differences between meshes 4 and 5 are found to be negligible, with mesh 5 ultimately selected for the subsequent phases of our study.

According to Schlichting & Klaus (2003), the estimations of the momentum and density boundary layers (l_m and l_d, respectively) are given by

$$l_m \sim O\left(\frac{D}{\sqrt{Re}}\right) \tag{3.6}$$

and

$$l_d \sim O\left(\frac{D}{\sqrt{Re\,Pr}}\right). \tag{3.7}$$

For stratified flows with $Pr > 1$, the boundary layer thickness is smaller for density than for velocity at a given Reynolds number. Thus a better-refined mesh is required for solving the density field. Based on (3.6) and (3.7), at the highest Reynolds number considered in our simulations ($Re_u = 356$, $Pr = 700$), the momentum and density boundary layer thicknesses are estimated to be $l_m \sim 0.053D$ and $l_d \sim 0.002D$, respectively, though our results indicate that the actual density boundary layer is thicker than this estimation. In

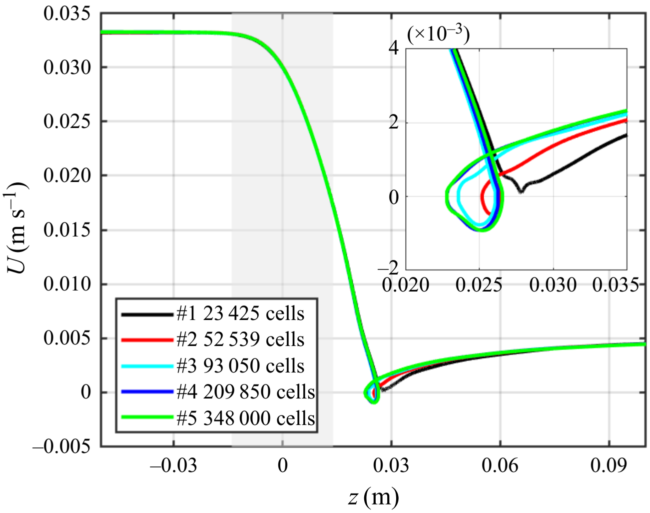

Figure 4. Velocity profiles of a settling particle at $Re_u = 198$, $Re_l = 26$ and $Fr = 2.3$, using five different meshes. The inset highlights the zone where bouncing occurs.

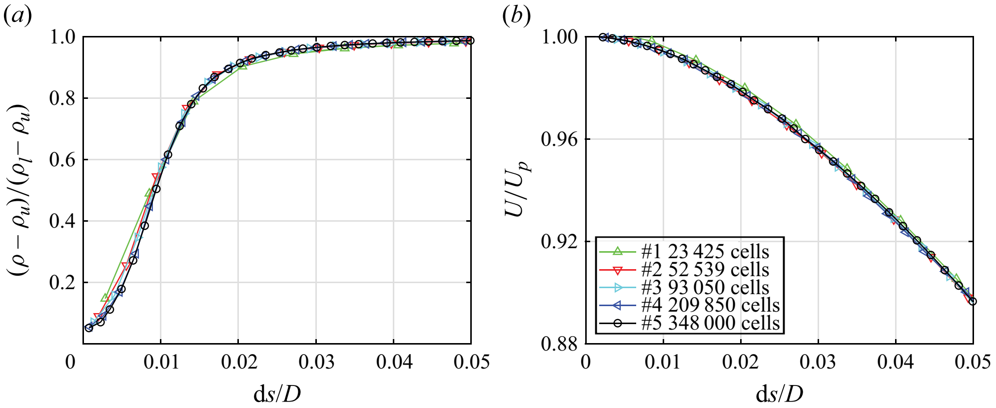

Figure 5. Variations of the dimensionless (*a*) density and (*b*) vertical velocity at the central axis near the lower particle surface when it reaches the lower bound of the density interface, considering $Re_u = 198$, $Re_l = 26$ and $Fr = 2.3$, using five different meshes. The distance from the particle surface is denoted by ds, and D is the particle diameter.

figure 6, we present the density field solved by mesh 5 at $Re_u = 356$, as the particle just passes the interface, and the density transition layer is compressed to be very thin. It is clear that the density boundary layer contains 5–7 cells. The density field within the boundary layer is well resolved using mesh 5. The mismatch of our numerical result and the estimation of (3.6) can be explained as follows. First, some previous studies pointed out that the actual thickness of the density boundary layer can be larger than the predicted value of (3.7) at moderate Reynolds numbers (Torres *et al.* 2000; Doostmohammadi *et al.* 2014*b*). Second, for a particle settling through a density interface, its velocity drops rapidly once it enters the density interface. The instant Reynolds number is smaller than Re_u, and the deceleration process also leads to a thicker boundary layer than that at a steady settling state.

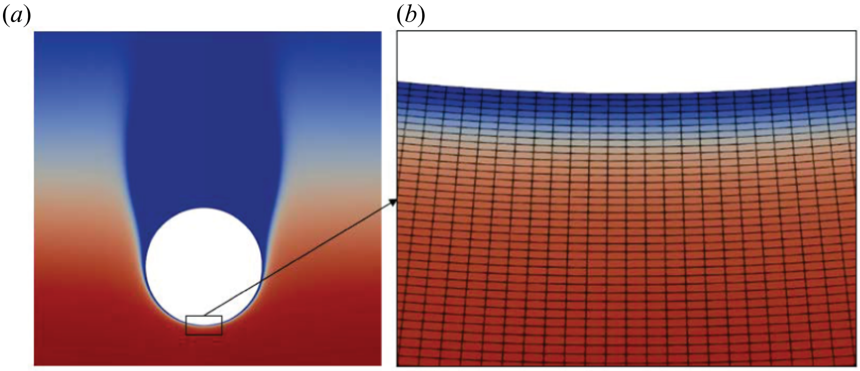

Figure 6. Density distribution surrounding the settling particle, along with a detailed view near the lower surface. The simulation is conducted using mesh 5 (refer to table 2) at Reynolds number $Re_u = 356$.

To test the influence of the domain size, we increase it to $35D \times 110D$ while keeping the grid distribution within the refined region unchanged. Compared to domain size $25D \times 90D$ (mesh 5), the velocity variations are respectively $+0.03\,\%$, $-0.59\,\%$ and $+1.09\,\%$ for U_u, U_l and U_{min}, supporting that the domain size of mesh 5 is acceptable for our numerical model.

We further compare our numerical results with experiments. Since the settling velocity is of primary importance in the current study and is determined by the physical properties of the system, we maintain the physical properties the same as in the experiments, and compare the variation of settling velocity. In a homogeneous fluid, we test the accelerating process of a particle settling from rest. The particle has diameter $D = 0.5$ mm and density $\rho_p = 2560\ \mathrm{kg\ m^{-3}}$, settling in fresh water (with kinematic viscosity $\nu = 8.9 \times 10^{-7}\ \mathrm{m^2 s^{-1}}$, density $998\ \mathrm{kg\ m^{-3}}$), corresponding to experiment 1 in Mordant & Pinton (2000). As shown in figure 7(a), the numerical and experimental velocities agree very well at the initial stage, and a terminal velocity $0.0773\ \mathrm{m\ s^{-1}}$ is reached, which has a discrepancy less than $4\,\%$ compared to the experimental value $0.0741\ \mathrm{m\ s^{-1}}$.

In a homogeneous fluid, the steady drag coefficient C_d can be estimated by the empirical formula

$$C_d = \frac{24}{Re} + \frac{6}{1+\sqrt{Re}} + 0.4, \tag{3.8}$$

with error less than $10\,\%$ for $0 < Re < 2 \times 10^5$ (White & Majdalani 2006). The terminal velocity predicted using (1.4) and (3.8) is $0.0765\ \mathrm{m\ s^{-1}}$, which is also plotted in figure 7(a) (the horizontal green dashed line). Our simulation shows good agreement with this prediction, with discrepancy $1.03\,\%$. In figure 7(b), the simulated drag coefficients C_d are presented, which agree with those predicted by (3.8).

Finally, we test our numerical model for a particle settling in a three-layer stratified fluid, and compare the results with our experiment. The physical parameters in the experiment are particle diameter $D = 1.0$ cm, particle density $\rho_p = 1126.36\ \mathrm{kg\ m^{-3}}$, upper-fluid density $\rho_u = 1119.42\ \mathrm{kg\ m^{-3}}$, lower-fluid density $\rho_l = 1125.90\ \mathrm{kg\ m^{-3}}$, interface thickness $L = 2.78$ cm, upper-fluid viscosity $\nu_u = 1.69 \times 10^{-6}\ \mathrm{m^2\ s^{-1}}$ and lower-fluid viscosity $\nu_l = 1.71 \times 10^{-6}\ \mathrm{m^2 s^{-1}}$. These physical parameters result in non-dimensional parameters $Re_u = 198$, $Re_l = 20$ and $Fr = 2.3$. Limited by our numerical method, the kinematic viscosity is uniform in the simulation. In figure 8, we present the settling

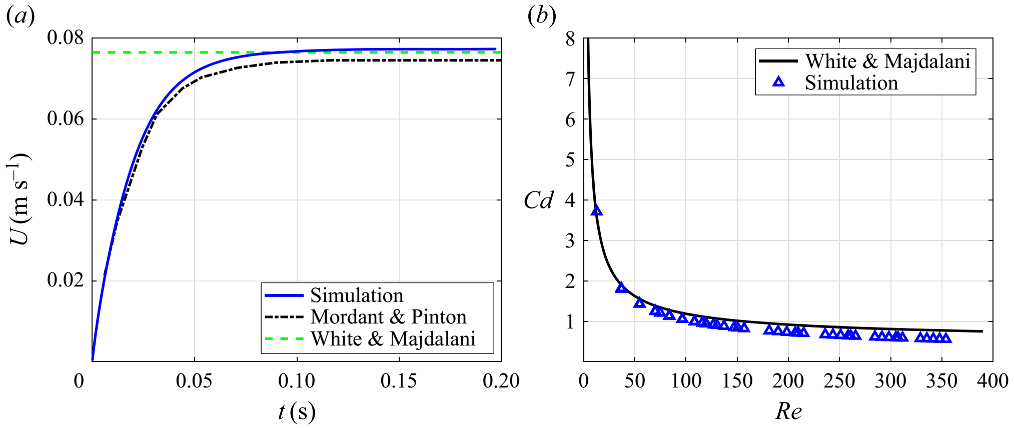

Figure 7. Validation of numerical simulations for homogeneous fluid. (*a*) Temporal variation of velocity for a settling particle (density 2560 kg m^{-3}, diameter 0.5 mm) in fresh water (density 998 kg m^{-3}, kinematic viscosity 8.9×10^{-7} m^2 s^{-1}). The blue solid line represents simulation results, the black dash-dotted line represents experimental data from Mordant & Pinton (2000), and the green dashed line represents the terminal velocity predicted using the drag law proposed by White & Majdalani (2006). (*b*) Variation of steady drag coefficients with Reynolds number. Blue triangles denote simulation data, and the black solid line represents the drag law proposed by White & Majdalani (2006).

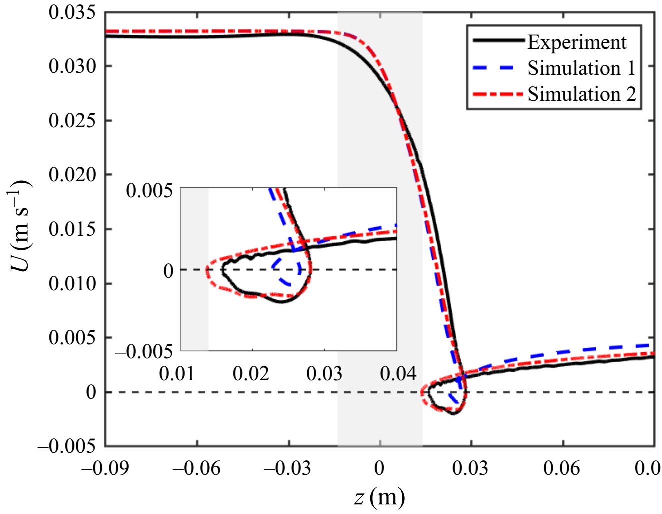

Figure 8. Velocity profiles of a particle settling in a stratified fluid with two different numerical set-ups – a comparison to our experiment.

velocities of the experiment compared with two simulation cases. Simulation 1 has the same physical parameters as the experiment, except that the uniform upper-layer viscosity is set to the whole domain, resulting in a higher Reynolds number, $Re_l = 26$. In simulation 2, the lower-layer density is adjusted slightly to match Re_l to the experiment. Both simulation cases successively predict the bouncing behaviour. Simulation 2 aligns better with the experiment when all the non-dimensional parameters (Re_u, Re_l, Fr) match the experiment.

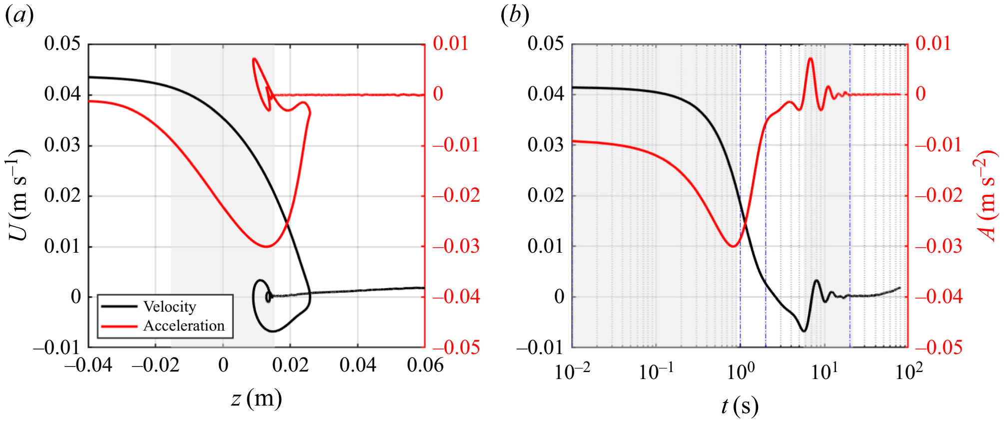

Figure 9. Settling velocity and acceleration of the particle with $Re_u = 347$, $Re_l = 20$ and $Fr = 2.5$ as functions of (*a*) vertical position and (*b*) settling time. The left- and right-hand vertical axes correspond respectively to the settling velocity and acceleration. In (*a*), the vertical position $z = 0$ refers to the middle plane of the transition layer, and the time $t = 0$ in (*b*) refers to the instant when the particle's centre reaches the upper boundary of the transition layer. In (*a*), the shaded region represents the transition layer, and in (*b*), the two shaded regions denote when the particle's centre is within the transition layer. Note that the right-hand shaded region in (*b*) denotes when the particle re-enters the transition layer after bouncing. In (*b*), four stages are divided by blue dashed lines.

4. Results and discussion

4.1. *Bouncing process*

First, we choose a typical set of parameters, to demonstrate the bouncing process of a particle settling through a density transition layer. This bouncing phenomenon, also known as levitation (Abaid *et al.* 2004), is detailed through the particle's velocity, acceleration and visualised flow patterns. In this subsection, the non-dimensional parameters are $Re_u = 347$, $Re_l = 20$ and $Fr = 2.5$. Under these Reynolds numbers, the flow is nearly axisymmetric, allowing the particle to remain within the laser-sheet-illuminated plane throughout the settling process and to be captured for observation.

The velocity and acceleration of the bouncing particle are depicted in figure 9. As illustrated in figure 9(*a*), the deceleration of the particle begins before it enters the density interface. This is due to the interface's presence, which limits the vertical displacement of the fluid (Ardekani & Stocker 2010). As the particle penetrates the interface, its velocity decreases more rapidly, with the maximum deceleration occurring at approximately the lower bound of the interface. The particle then reaches a zero velocity in the lower layer and bounces up, re-entering the interface. The bouncing is akin to the beginning of a damped oscillation, which is more obvious in figure 9(*b*). Note that this oscillation is not a common feature of a bouncing particle. It occurs only in strong bouncing scenarios where the particle can re-enter the interface. Finally, the particle accelerates again and gradually approaches its new terminal velocity.

A series of images, corresponding to figure 9, showing the wake development during the entire settling process, are presented in figure 10. The settling process is divided into four stages, as indicated by vertical dashed lines in figure 9(*b*), and the corresponding wake behaviour is observed in each stage. The four stages are as follows.

(1) Wake attachment (figures 10*a*–*e*). As the particle enters the interface, a large amount of upper fluid is dragged by the particle, creating an attached wake. The velocity of

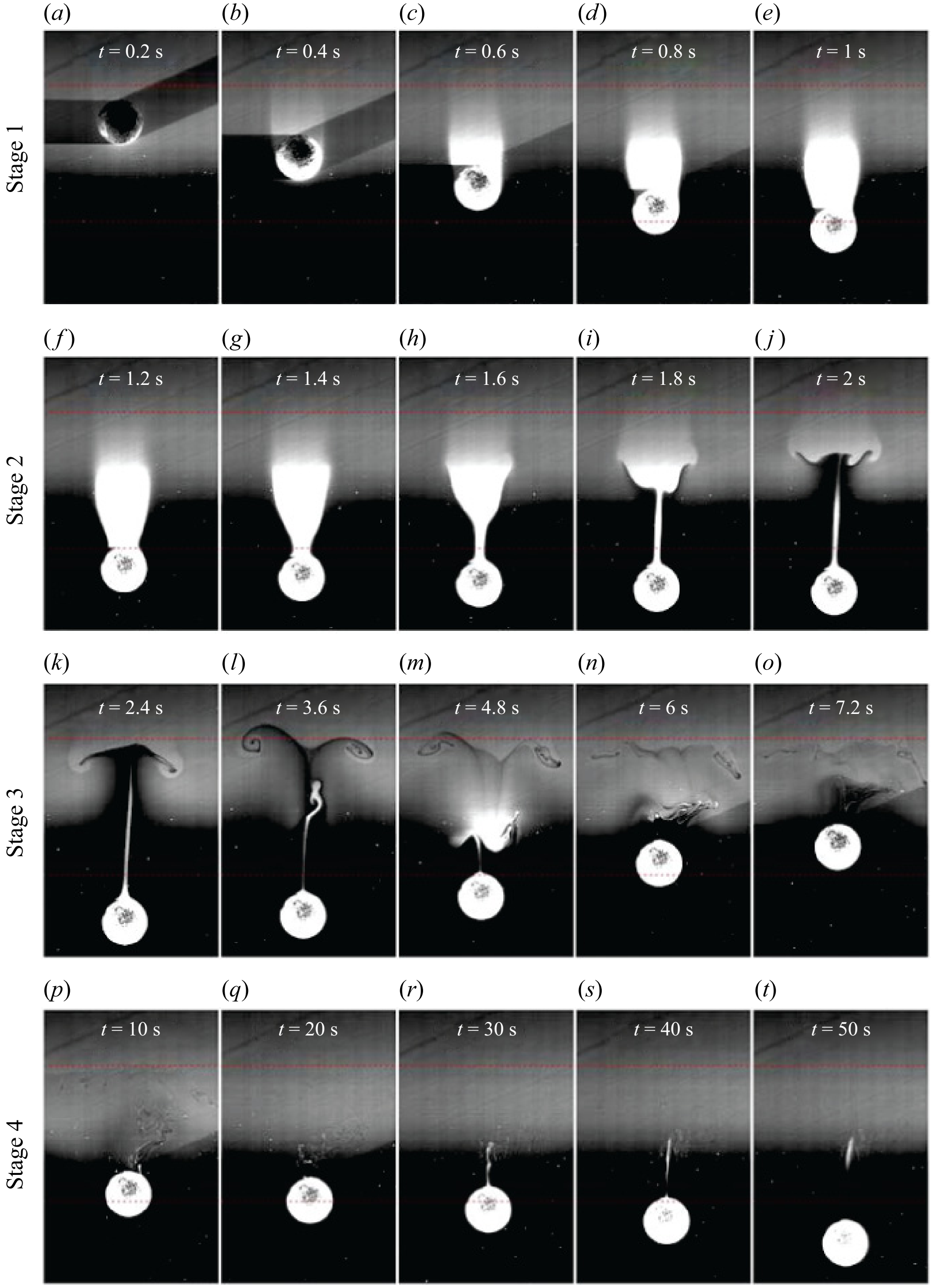

Figure 10. A sequence of images showing the bouncing process of a particle settling through a density transition layer, corresponding to figure 9. The two red dashed lines in each image represent the bounds of the interface. The non-dimensional parameters are $Re_u = 347$, $Re_l = 20$ and $Fr = 2.5$.

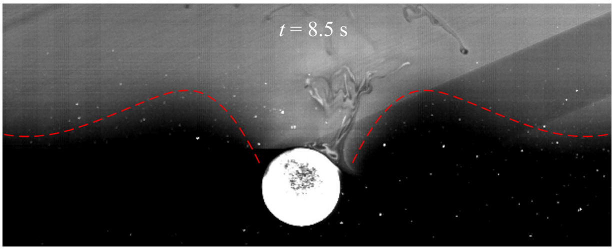

Figure 11. Full image of the internal wave at $t = 8.5$ s between figures 10(o) and 10(p).

the particle decreases rapidly, and the deceleration reaches its maximum at the end of this stage (figure 9b).

(2) Wake detachment (figures 10f–j). At this stage, most of the attached wake detaches from the particle and returns to its neutral position. A long, thin column of lighter fluid remains attached to the centre axis above the particle. As the volume of attached lighter fluid decreases due to the wake detachment, the extra buoyancy diminishes, resulting in a reduced contribution to the stratification drag (refer to the variation of F_{sb} in figure 17). Concurrently, the particle's velocity continues to decline, and the acceleration diminishes compared to the first stage (figure 9b). By the end of this stage, the particle loses over 90 % of its initial entering velocity U_u.

(3) Transient bouncing (figures 10k–q). The particle comes to a halt (at $t = 2.61$ s) and rebounds upwards. As the bouncing event approaches, the particle's instantaneous vertical velocity $U(t)$ decreases to near zero, resulting in a small Froude number $Fr(t) = U(t)/ND \ll 1$. This situation could lead to the formation of a thin jet, akin to type A reported by Hanazaki *et al.* (2009), as depicted in figure 5(k) ($t = 2.4$ s). Furthermore, a strong internal wave emerges at the interface, triggered by the rupture of the wake (figure 11). Nearly all the lighter fluid has detached from the particle by this stage, evidencing a minimal contribution of the extra buoyancy from the dragged light fluid to the drag during the bouncing event. This observation aligns with the force decomposition findings detailed in § 4.3.3.

(4) Final sedimentation (figures 10r–t). Following the bouncing and subsequent oscillation, the particle gradually descends to the bottom of the tank. Although it is challenging to discern in figures 10(n–q) before detachment from the particle surface, a small amount of light fluid persists at the particle surface. Note the extended time interval between images. During this phase, the particle settles extremely slowly after traversing the density interface. At $t = 50$ s, its velocity restores to approximately 30 % of the terminal velocity in the homogeneous lower layer.

These four stages are representative of the typical settling process experienced by a bouncing particle. It is important to note that the actual bouncing process begins only at the third stage, after the wake has detached from the particle. This is consistent with the observations made by Abaid *et al.* (2004) that the particle changes its direction of motion after the rising of the 'plume', which in our experiment corresponds to the detached wake. For a monotonically settling particle, the first two stages are identical to those experienced by the bouncing particle, but are followed by a final sedimentation without any bouncing motion.

4.2. *Flow structure*

To investigate the transient flow structure around the particle, PIV measurement and flow visualisation are conducted simultaneously, using experimental set-up 2 (see figure 1*b*). In figure 12, we present the results of a particle with $\rho_p = 1126.06\ \mathrm{kg\ m^{-3}}$, bouncing in a stratified fluid with densities $\rho_u = 1119.37\ \mathrm{kg\ m^{-3}}$ and $\rho_l = 1125.77\ \mathrm{kg\ m^{-3}}$, and interface thickness $L = 3.47$ cm. These correspond to non-dimensional parameters $Re_u = 248$ and $Fr = 2.49$. As the particle exits the camera's field of view, we estimate $Re_l = 15$, although this is likely an underestimate due to the limited view size ($9.4 \times 7.3\ \mathrm{cm^2}$) utilised in this experiment.

Initially, the flow around the particle is similar to that in a homogeneous fluid. However, after the particle enters the interface, accompanying the rupture of the wake, a vortex with direction opposite to that in the homogeneous fluid is formed at the rear of the particle. This vortex grows quickly and detaches from the particle, becoming a vortex ring that remains at the interface (figures 12*d*,*e*). As previous research has explained (Zhang *et al.* 2019; Magnaudet & Mercier 2020), this vortex is sourced from the baroclinic torque caused by the misalignment between the density and pressure gradients.

Figure 13 presents a close-up view of the vertical velocity distribution around the particle, clearly showing a strong upward flow, referred to as a jet hereafter, formed behind the particle before bouncing occurs (figures 13*c*–*i*). The formation of the jet is a transient process. Initially, the jet forms in a U-shaped region (13*c*) and then develops towards the central axis. It reaches maximum strength at approximately $1.5D$ above the particle, when the main part of the wake detaches (figure 13*d*). Subsequently, it transforms into a long, thin jet at the rear of the particle, and a bell-shaped structure (yellow region in figure 13*i*), similar to type A of Hanazaki *et al.* (2009), is observed at the end of the jet. It is worth noting that there is a time lag from the formation of the jet to the bouncing of the particle. It is evident in figure 13 that when the maximum jet is formed at 2.4 s, there is a region of downward fluid surrounding the particle. The jet touches the upper particle surface at $t = 3.6$ s in figure 13(f); until then, it could affect the particle motion directly.

4.3. *Force analysis*

In this subsection, we analyse the forces acting on a bouncing particle to gain a more in-depth understanding of the bouncing behaviour. The non-monotonic motion of a particle settling in a stratified fluid is known to be caused by the so-called 'stratification drag' (denoted F_s). Previous studies have shown that in steady or quasi-steady states, F_s is contributed to mainly by two mechanisms: the buoyancy of the dragged upper fluid (F_{sb}), and the force caused by a specific flow structure (F_{sf}) (Srdić-Mitrović *et al.* 1999; Higginson *et al.* 2003; Yick *et al.* 2009; Zhang *et al.* 2019). Here, we decompose the total force and quantify the contributions of F_{sb} and F_{sf}, using a combined numerical and empirical force decomposition method based on the strategy used by Srdić-Mitrović *et al.* (1999) and Zhang *et al.* (2019).

Our force analysis consists of three steps. First, we describe how we decompose the force. Second, we explain how we calculate the force components. Finally, we present the transient forces acting on a bouncing particle, and analyse the bouncing mechanism.

4.3.1. *Force decomposition*

To understand the underlying physics of particle bouncing behaviour, we aim to decompose its hydrodynamic force into different components. We begin with the motion

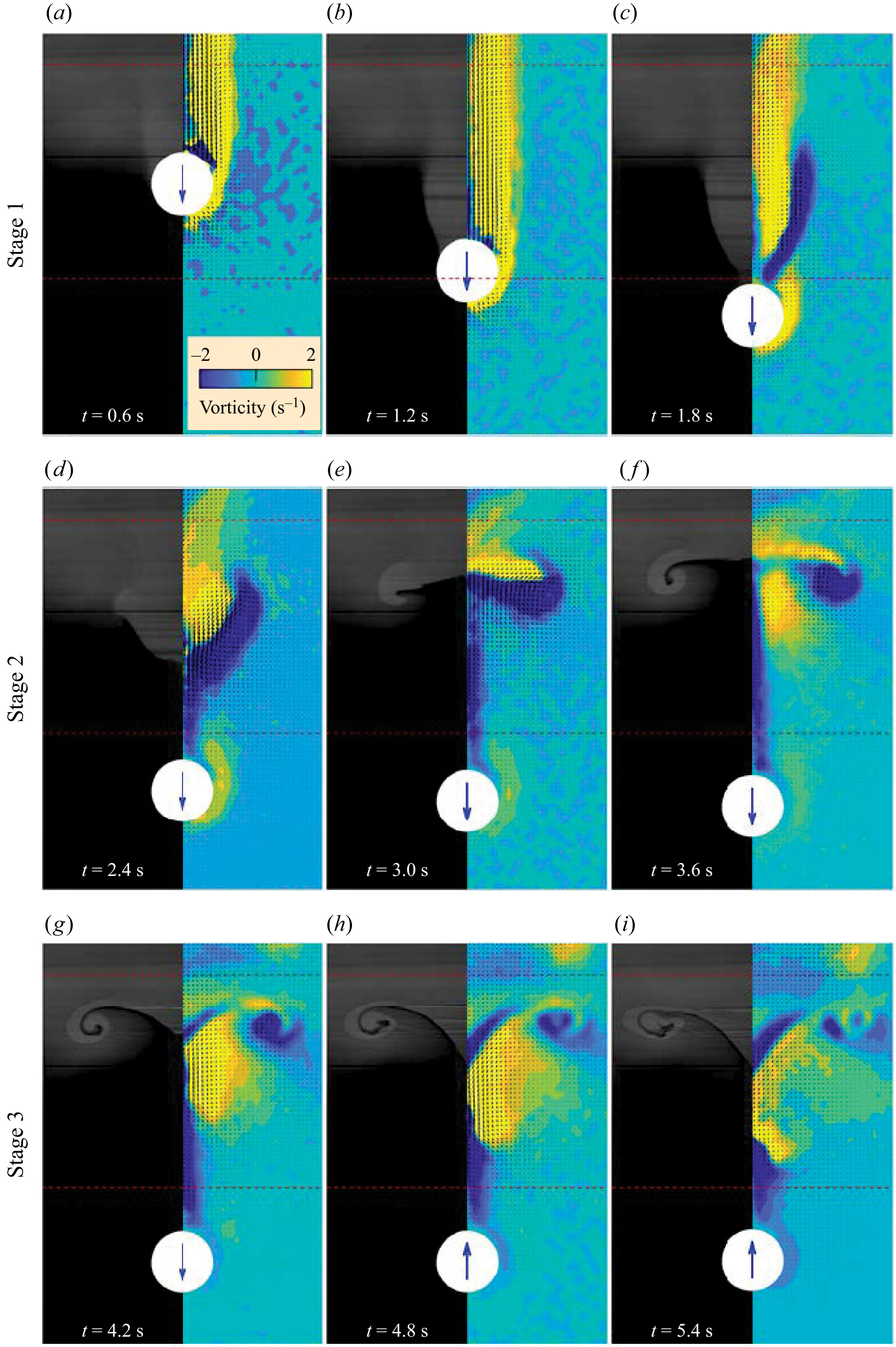

Figure 12. Illuminated wake (left-hand part of each image) and PIV field (right-hand part) of a particle settling through a density transition layer at $Re_u = 248$, $Fr = 2.49$ and $Re_l = 15$. The horizontal red dashed lines mark the bounds of the interface. The arrow at the particle centre indicates the direction of its motion.

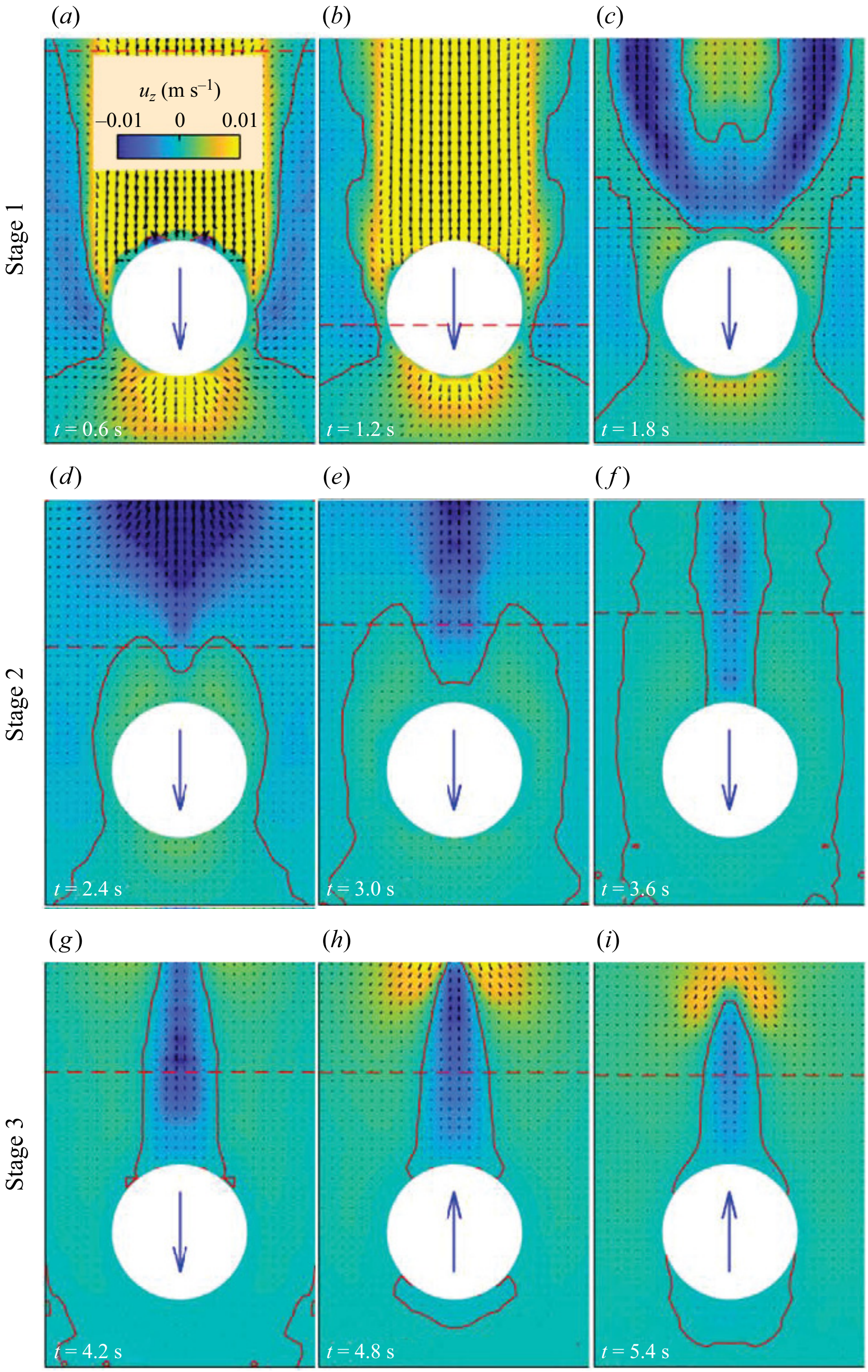

Figure 13. A close-up view of the flow field around the particle, corresponding to figure 12. An upward jet is observed at the centre axis behind the particle just before it changes its direction of motion. The isolines of $u_z = 0$ are depicted as red solid lines, which separate the region with positive and negative vertical velocities. The horizontal red dashed line in (*a*) indicates the upper boundary of the interface, while in (*b*–*i*) it denotes the lower boundary of the interface. The arrow at the particle centre indicates the direction of its motion.

equation of a particle settling from rest in a quiescent, homogeneous fluid, which can be written as

$$m_p \frac{\mathrm{d}U}{\mathrm{d}t} = G + F_b + F_d + F_a + F_h. \tag{4.1}$$

The left-hand side represents the total inertia force acting upon the particle, where m_p is the particle mass. This arises due to the imbalance of forces. On the right-hand side, G and F_b are respectively the gravity and buoyancy forces of the particle, and the sum $G + F_b$ is the reduced gravity of the particle; F_d is the steady drag force at the considered time instant, F_a is the inertia force of added mass, and F_h is the history (Basset) force. Here, F_d can be evaluated according to (1.2) and (3.8). In the limit of potential flow, F_a can be calculated as

$$F_a = -\frac{1}{2} \rho_f V_p \frac{\mathrm{d}U}{\mathrm{d}t}. \tag{4.2}$$

At the Stokes regime, F_h has an analytic solution:

$$F_h = -\frac{3}{2} D^2 \sqrt{\pi \rho_f \mu} \int_{-\infty}^{t} \frac{\dot{U}(\tau)}{\sqrt{t-\tau}} \, \mathrm{d}\tau. \tag{4.3}$$

Although (4.2) and (4.3) do not fit the current parameter range, they demonstrate that the directions of F_a and F_h are opposite to the acceleration. For a decelerating particle, they behave as thrust rather than drag. For a particle settling in a stratified fluid, we follow the same method of drag force decomposition as in (4.1), while introducing an extra term F_s to account for the stratification effects. The motion equation becomes

$$m_p \frac{\mathrm{d}U}{\mathrm{d}t} = G + F_b + F_d + F_a + F_h + F_s. \tag{4.4}$$

It is reasonable to further decompose F_s into two components,

$$F_s = F_{sb} + F_{sj}, \tag{4.5}$$

where F_{sb} represents the enhanced buoyancy caused by dragging the upper fluid to the lower layer, thus modifying the density distributions, while F_{sj} is the force caused by the induced flow structure due to the stratification, typically represented by the upward jet flow at the rear of the particle, as observed in figure 13. This upward jet is conjectured to be the dominant flow structure as the particle bounces. Therefore, the equation of motion for a particle settling in a stratified fluid can be written as

$$m_p \frac{\mathrm{d}U}{\mathrm{d}t} = G + F_b + F_d + F_a + F_h + F_{sb} + F_{sj}. \tag{4.6}$$

4.3.2. *Force calculation*

In this subsubsection, we introduce how we calculate the force components. First, we rearrange (4.6) as

$$m_p \frac{\mathrm{d}U}{\mathrm{d}t} = G + \underbrace{(F_b + F_{sb})}_{F_{static}} + \underbrace{(F_d + F_a + F_h + F_{sj})}_{F_{dynamic}}. \tag{4.7}$$

Here, the total hydro-force F_{hydro} is split into two parts: F_{static} and $F_{dynamic}$, where F_{static} refers to the hydrostatic force arising from the non-uniform density distribution with zero velocity, whereas $F_{dynamic}$ pertains to the force resulting from the non-zero velocity field at a uniform density distribution. Excluding the steady drag F_d, we note that $F_{sf} = F_a + F_h + F_{sj}$ represents the force caused by unsteady flow, i.e. the flow induced by the stratification effect.

In numerical simulation, the velocity, pressure and density fields are obtained by solving (3.1), (3.2), and (3.3). The total hydro-force F_{hydro} acting on the particle can be calculated using (3.4). The pressure can be divided into two components, $p = p_s + p_d$, where p_s denotes the hydrostatic pressure caused by the non-uniform density distribution, and p_d represents the pressure caused by flow. As the density field is known, p_s can be obtained by solving the equation

$$\nabla p_s = \rho \boldsymbol{g}. \tag{4.8}$$

Then F_{static} is calculated as the integration of p_s over the particle surface:

$$F_{static} = -\int_S p_s \boldsymbol{n}\,\mathrm{d}S, \tag{4.9}$$

and $F_{dynamic}$ is obtained using

$$\begin{aligned} F_{dynamic} &= F_{hydro} - F_{static} && (4.10)\\ &= -\int_S p_d \boldsymbol{n}\,\mathrm{d}S - \int_S \mu(\nabla \boldsymbol{u} + \nabla \boldsymbol{u}^{\mathrm{T}}) \boldsymbol{\cdot} \boldsymbol{n}\,\mathrm{d}S. && (4.11) \end{aligned}$$

With the density distribution following (2.1), the undisturbed hydrostatic pressure is given by

$$\begin{aligned} p_b &= \int \rho g\,\mathrm{d}z = \frac{1}{2} g(\rho_u + \rho_l)(z - z_{ref}) \\ &\quad + \frac{1}{2} g(\rho_u - \rho_l)\left[(z - z_{ref})\,\mathrm{erf}(\alpha(z - z_{ref})) + \frac{1}{\alpha\sqrt{\pi}} \exp(-(\alpha(z - z_{ref}))^2)\right]. \end{aligned} \tag{4.12}$$

We can obtain F_b, denoting the buoyancy of the particle in the undisturbed density field, by integrating p_b over the particle surface. Then the contribution of F_{sb} is quantified using

$$F_{sb} = F_{static} - F_b. \tag{4.13}$$

Upon evaluating the steady drag F_d through (1.2) and (3.8), the drag component arising from unsteady flow can be expressed as

$$F_{sf} = F_{sj} + F_a + F_h = F_{dynamic} - F_d. \tag{4.14}$$

Force calculation can also be conducted using the experimental data, with only two steps different from the simulation, as follows.

(1) The hydro-force is calculated using

$$F_{hydro} = G - m_p A, \tag{4.15}$$

where A is the acceleration of the particle, obtained by taking the second derivative of the particle position.

(2) The density field is reconstructed using the flow visualisation images (left-hand of each image in figure 12), similar to the laser-induced fluorescence method used by Okino *et al.* (2021). The grey value in these images, representing the concentration of the Rhodamine B dye, is linearly transformed to density. The hydrostatic pressure p_s is then calculated using these reconstructed density fields. The other steps are the same as those for dealing with the simulation data.

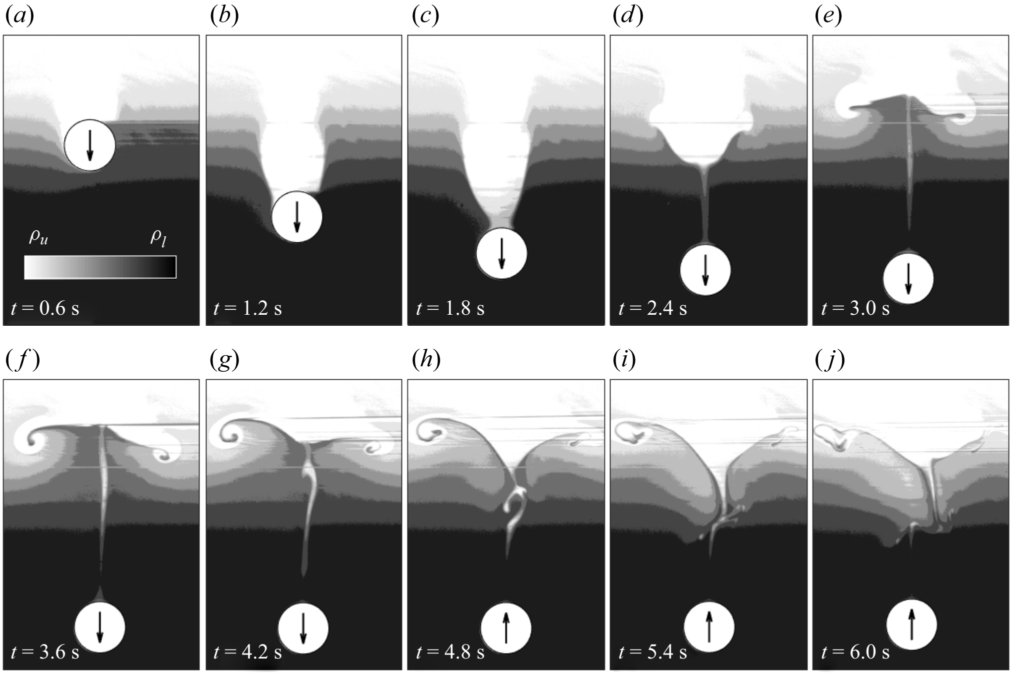

Figure 14. Reconstructed density field using flow visualisation images from the corresponding experiments shown in figure 12.

4.3.3. *Forces of a bouncing particle*

In this subsubsection, we analyse the forces observed in the experiments presented in figure 12, with the reconstructed density fields presented in figure 14. A comparison is made to the simulated results as shown in figure 15. Overall, the evolution of flow structures is consistent between the two methods. The simulation reveals that a small amount of lighter fluid detaches and ascends from the particle surface to the upper layer as bouncing occurs (figures 15*h*–*j*). This phenomenon, termed 'secondary detachment' and discussed in Wang, Wang & Deng (2023), occurs at thin interfaces and high Re_u. Although not captured in the current experiment (figure 14), it was observed in our recent experiments for larger particles with diameters exceeding 2 cm (not presented here).

Figure 16 compares velocity profiles between the experiment and simulation. Limited by the camera view, the particle has not reached its terminal velocity by the end of the experiment, resulting in $Re_l = 15$ as it exits the view. In contrast, in the simulation, the particle reaches a higher velocity, resulting in $Re_l = 28$.

The decomposed forces are depicted in figure 17, showing simulation (figures 17*a*,*b*) and experiment (figures 17*c*,*d*) results. The variation of force components shows good agreement. Before entering the transition layer, the particle settles at a constant velocity due to the balance between reduced gravity ($G + F_b$) and the drag force F_d. As the particle enters the transition layer, the force components $m_p\,\mathrm{d}U/\mathrm{d}t$, F_{sb} and F_{sf} gradually increase from nearly zero values (figures 17*a*,*c*). In figure 17(*d*), F_{sf} initially shows a negative value, inconsistent with the simulation (figure 17*b*). This discrepancy may be attributed to the error in calculating the acceleration during the experiment, as the acceleration magnitude observed in the experiment (see the black line in figure 17*d*) is slightly larger than in the simulation at the beginning.

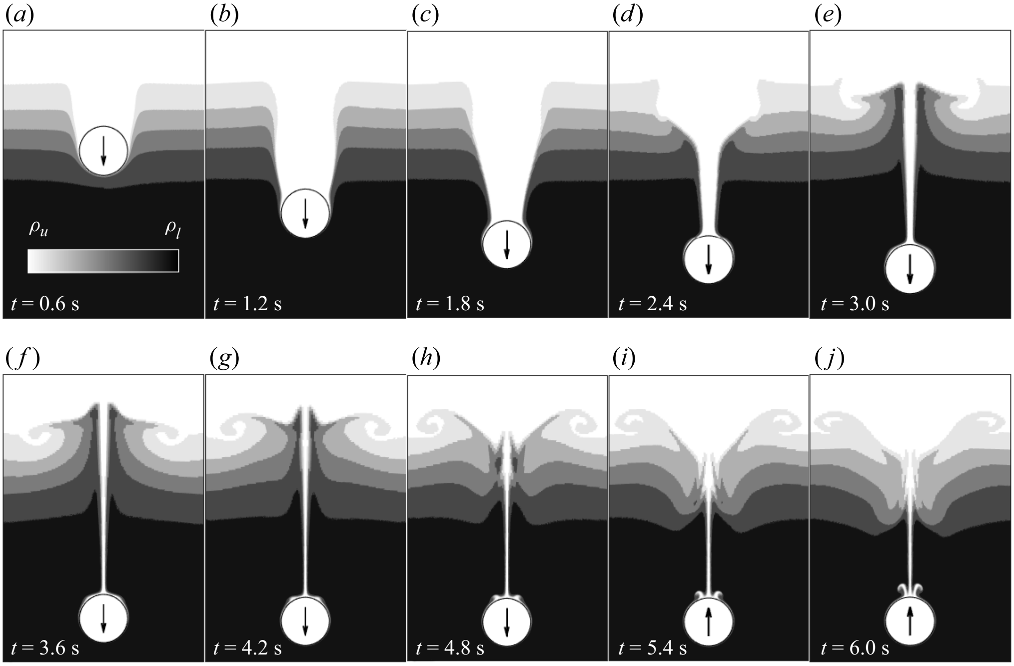

Figure 15. Simulated density field, using the same physical parameters as the experiment depicted in figure 12, presented for comparison with figure 14.

Different stages are separated by vertical blue dashed lines in figures 17(*b*) and 17(*d*). The wake buoyancy force F_{sb} correlates with the volume of attached upper light fluid. It reaches a maximum at the end of the first stage, after the dragging of the wake (see figures 14(*b*) and 15(*b*) at $t = 1.2$ s), just before the wake detaches from the particle. The sudden deceleration of the particle causes the sharp rise in F_{sf} due to the inertia, acting as a thrust (positive value) in the first stage. As the particle approaches the third stage, F_{sb} decreases as only a thin layer of light fluid remains in the attached wake (see figures 14(*f*) and 15(*f*) at $t = 3.6$ s). Meanwhile, F_{sf} becomes the dominant drag force, balancing the reduced gravity $(G + F_b)$ and preventing further settling of the particle.

When a particle settles through a density interface and $U_{min} \leqslant 0$ (with the positive direction of the z-axis pointing downwards), the particle bounces up. At the instant of bouncing (the first time $U = 0$, indicated by the arrow in figure 16), the particle satisfies the conditions

$$U = 0, \quad \frac{\mathrm{d}U}{\mathrm{d}t} < 0. \tag{4.16a,b}$$

Therefore, we have

$$m_p \frac{\mathrm{d}U}{\mathrm{d}t} = \underbrace{G + F_b}_{+} + \underbrace{F_d}_{0} + \underbrace{F_a}_{+} + \underbrace{F_h}_{+} + \underbrace{F_{sb}}_{-} + \underbrace{F_{sj}}_{-} < 0. \tag{4.17}$$

The necessary condition for (4.17) to hold is given by

$$|F_{sb}| + |F_{sj}| > |G + F_b|. \tag{4.18}$$

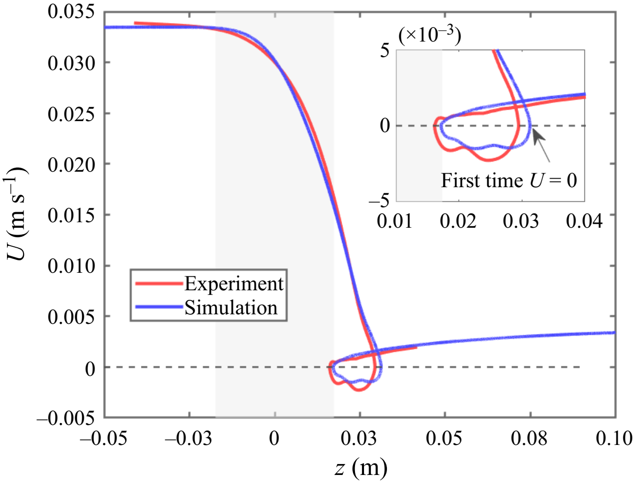

Figure 16. Comparison between the simulated and experimental velocity profiles of a particle with density $\rho_p = 1126.06$ kg m^{-3} and diameter $D = 1$ cm, bouncing in stratified fluid with upper and lower densities $\rho_u = 1119.37$ kg m^3 and $\rho_l = 1125.77$ kg m^{-3}, respectively, over an interface of thickness $L = 3.47$ cm. The resulting non-dimensional parameters are $Re_u = 248$ and $Fr = 2.49$. The lower Reynolds numbers using the end velocities of the experiment and simulation are respectively $Re_l = 15$ and $Re_l = 28$.

Whether the jet is necessary for the occurrence of bouncing depends on the magnitude of F_{sb}. When $|F_{sb}| \leqslant |G + F_b|$, the contribution of the jet is necessary for the bouncing behaviour.

In figures 17(*b*) and 17(*d*), at the instant of bouncing occurrence (marked by the black dashed line), F_{sf} plays a dominant role in balancing the reduced gravity. Excluding the positive contribution from $(F_a + F_h)$, F_{sj} becomes the primary component of the drag force. It is important to note that in the current study, F_{sj} refers to the force generated by the relative upward flow around the particle, encompassing both pressure and viscosity contributions. This differs from the approach taken by Zhang *et al.* (2019), who decomposed the stratification force into three parts: (1) Archimedes drag arising from the entrainment of the lighter fluid, equivalent to F_{sb} in our study; (2) inertial force due to the momentum force induced by density disturbances (pressure contribution); and (3) shear force acting on the particle surface induced due to baroclinic vorticity (viscosity contribution). In our scenario, the particle's velocity undergoes rapid fluctuations, leading to swift alterations in the steady drag F_d. This makes it challenging to accurately quantify the transient effects of pressure and viscosity on F_d, thus precluding further decomposition of F_{sj} into inertia-induced and viscosity-induced stratification forces.

In summary, the mechanism of the bouncing phenomenon is understood as follows. At the early stage, F_{sb} dominates the drag force due to the large amount of attached light fluid, causing the particle to lose most of its initial velocity. After the particle enters the lower layer, the light fluid detaches and produces an upward jet. Then F_{sb} decreases, and the contribution of F_{sj} to the drag increases and becomes dominant, causing the particle to continue to decelerate until it bounces up.

4.4. *Influence of different parameters*

To investigate the impact of various parameters, we conducted three experimental series, each consisting of five tests, as outlined in table 3. By adjusting the densities of the

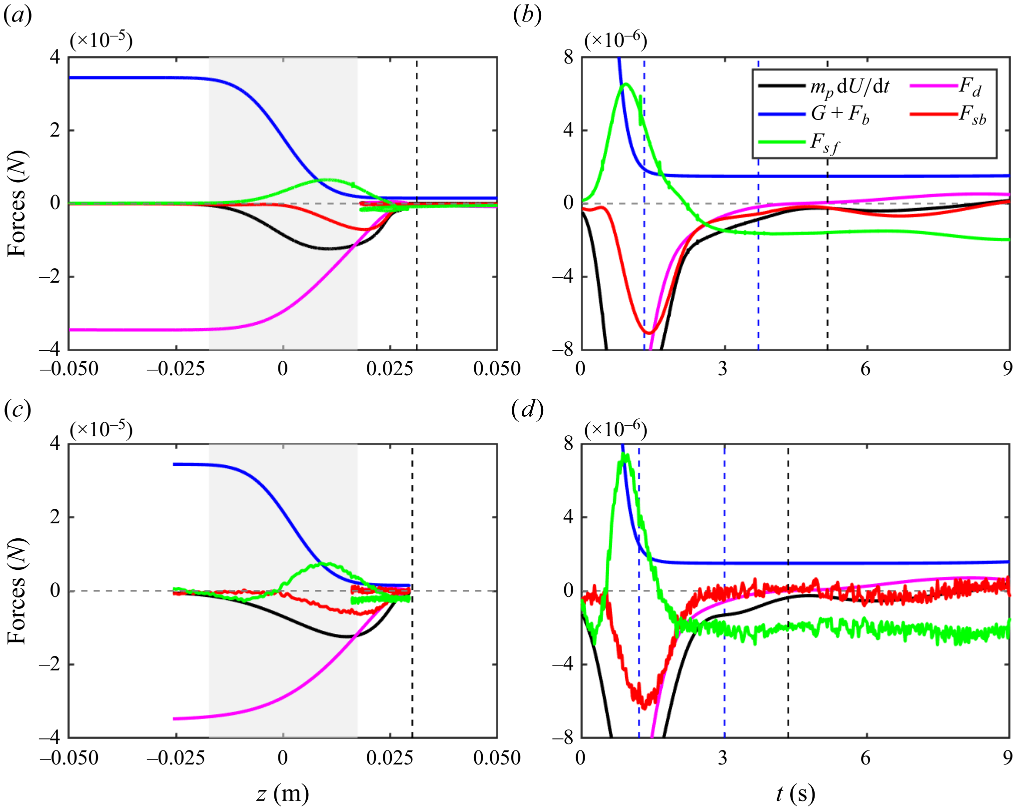

Figure 17. Decomposed forces acting on a bouncing particle corresponding to the experiment depicted in figure 12, as well as that from the simulation using the same set of parameters: (*a*,*b*) forces computed from numerical simulation data; (*c*,*d*) forces derived from experimental data. The shaded areas in (*a*,*c*) indicate the interface region, with the black dashed lines denoting the initiation of bouncing behaviour. In (*b*,*d*), different stages of the particle's motion are delineated by blue dashed lines: wake attachment (from $t = 0$ to the first blue dashed line), wake detachment (from the first to the second blue dashed lines), transient bouncing (from the second blue dashed line to the end). The final sedimentation stage is not depicted in these plots.

lower (ρ_l) and upper (ρ_u) fluids, and the thickness of the interface layer (L), we varied the lower-layer Reynolds number (Re_l), upper-layer Reynolds number (Re_u) and Froude number (Fr). For each test, we released five particles with slightly different properties, as detailed in table 4. The minimum velocity (U_{min}) attained by each particle during its sedimentation is presented in table 3. A negative U_{min} indicates that the particle experienced a bouncing motion. Prior to each test, we accurately measured the density of the particle to within 0.01 kg m^{-3}, as the density of the particle varies with ambient temperature.

Figure 18 displays the non-dimensional minimal velocity (U_{min}/U_u) as a function of Re_l, Re_u, and Fr, using all the experimental data collected. It is evident that U_{min}/U_u exhibits a stronger correlation with Re_l ($1 \leqslant Re_l \leqslant 109$) compared to Re_u ($152 \leqslant Re_u \leqslant 322$) and Fr ($2.3 \leqslant Fr \leqslant 5.6$). Notably, bouncing is observed when Re_l is less than approximately 30.

				Minimal velocity (cm s^{-1})					Re_u					Re_l					Fr				
Experiment series	ρ_u (kg m^{-3})	ρ_l (kg m^{-3})	L (cm)	P1	P2	P3	P4	P5	P1	P2	P3	P4	P5	P1	P2	P3	P4	P5	P1	P2	P3	P4	P5
Series 1	1116.52	1123.66	3.14	−0.492	−0.228	0.304	0.578	0.889	246	247	253	255	268	5	29	50	65	81	2.5	2.5	2.6	2.6	2.7
	1116.52	1123.32	3.01	−0.140	0.237	0.560	0.780	1.048	239	247	252	255	265	31	47	64	77	91	2.4	2.5	2.6	2.6	2.7
	1116.52	1123.01	2.92	0.250	0.468	0.735	0.952	1.218	236	244	250	254	265	47	60	75	87	100	2.4	2.5	2.6	2.6	2.7
	1116.55	1122.71	2.86	0.415	0.610	0.858	1.059	1.302	238	247	246	253	265	59	71	85	96	109	2.5	2.6	2.6	2.6	2.8
	1116.52	1122.39	2.52	0.683	0.835	1.067	1.249	1.467	238	248	248	254	262	72	82	95	106	117	2.4	2.5	2.5	2.6	2.6
Series 2	1115.05	1121.87	2.71	−0.397	0.015	0.454	0.712	0.994	261	270	273	281	294	13	31	48	65	84	2.3	2.4	2.4	2.5	2.6
	1115.90	1121.85	3.22	−0.324	0.114	0.497	0.739	1.025	242	248	255	266	273	15	32	51	68	88	2.5	2.5	2.6	2.7	2.8
	1116.86	1121.85	3.23	−0.414	−0.100	0.376	0.648	0.939	214	223	231	240	249	4	27	44	61	81	2.4	2.5	2.6	2.7	2.8
	1117.97	1121.95	3.02	−0.337	0.064	0.475	0.742	1.022	185	195	206	215	227	5	27	48	66	86	2.3	2.4	2.5	2.6	2.8
	1118.63	1121.45	3.67	−0.162	0.137	0.516	0.781	0.985	152	164	177	189	198	8	28	51	70	85	2.4	2.6	2.8	3.0	3.1
Series 3	1113.93	1122.24	3.15	−0.559	−0.214	0.336	0.616	0.879	282	297	298	301	314	13	32	44	59	76	2.5	2.6	2.6	2.6	2.8
	1113.92	1122.24	6.72	−0.248	−0.087	0.376	0.651	0.922	290	294	303	308	314	13	30	47	62	80	3.7	3.7	3.9	3.9	4.0
	1113.92	1122.24	9.83	−0.117	0.014	0.371	0.639	0.928	290	298	305	305	319	12	28	44	60	78	4.4	4.5	4.7	4.7	4.9
	1113.92	1122.24	11.53	−0.035	0.103	0.435	0.705	0.954	288	296	305	311	322	9	26	43	59	76	4.8	4.9	5.0	5.2	5.4
	1113.92	1122.24	13.06	0.013	0.118	0.461	0.724	0.993	281	290	303	304	315	11	25	41	58	75	5.0	5.1	5.4	5.4	5.6

Table 3. Experimental parameters and minimal velocities.

Particle number	Diameter (mm)	Density (kg m^{-3})
P1	10.075	1121.58–1123.74
P2	10.128	1121.86–1124.00
P3	10.083	1122.28–1124.60
P4	10.075	1122.73–1124.79
P5	10.055	1123.18–1125.26

Table 4. Particle properties.

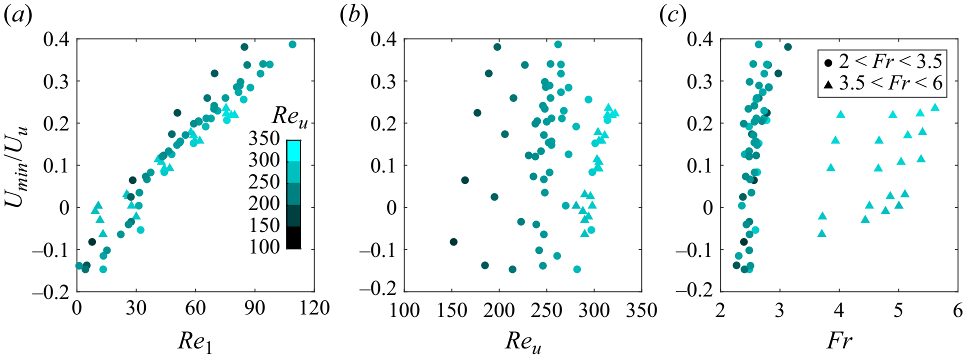

Figure 18. The minimal velocity of all the particles in experiments versus lower and upper Reynolds numbers, and Froude number. Here, $U_{min}/U_u < 0$ represents the occurrence of a bouncing motion.

4.4.1. *Lower Reynolds number Re_l*

To investigate the correlation between the minimal velocity and the lower Reynolds number further, we analyse the experimental data from series 1, where the upper Reynolds number and Froude number are $Re_u = 252 \pm 16$ and $Fr = 2.6 \pm 0.2$, respectively. In figure 19(*a*), we plot these experimental results against the lower Reynolds number Re_l. We also include numerical results at fixed Froude number $Fr = 2.6$ and upper Reynolds numbers $Re_u = 258$ and $Re_u = 349$ for comparison.

Both the experimental and numerical results demonstrate that U_{min}/U_u increases linearly with Re_l. We note that for $Re_u \sim 252$, the values of U_{min}/U_u in the experiments are uniformly higher than those in the simulations at a similar $Re_u \sim 258$. This discrepancy is possibly caused by the incomplete development of U_l in the experiments. The velocity measured when the particle exits the viewing window may be smaller than the fully developed U_l in the simulations, leading to a smaller Re_l. To fit the data in figure 19(*a*), we employ the linear expression

$$\frac{U_{min}}{U_u} = c_1\, Re_l + c_2. \tag{4.19}$$

Our linear regression analysis yields $c_1 = 0.0049$ and $c_2 = -0.1181$ for the experiments ($Re_u = 252 \pm 16$), and $c_1 = 0.0046$ and $c_2 = -0.1720$ for the numerical results ($Re_u = 258$). We identify critical lower Reynolds numbers $Re_l^* = 23.9$ and 37.5 for these two lines, respectively. These critical Reynolds numbers correspond to the position where $U_{min} = 0$. The values of c_1 and c_2 are dependent on Re_u and Fr. In figure 19(*a*), we observe that a higher upper Reynolds number $Re_u = 349$ leads to a smaller c_1 compared to both the experiments and simulations with smaller Reynolds numbers. However, we also note

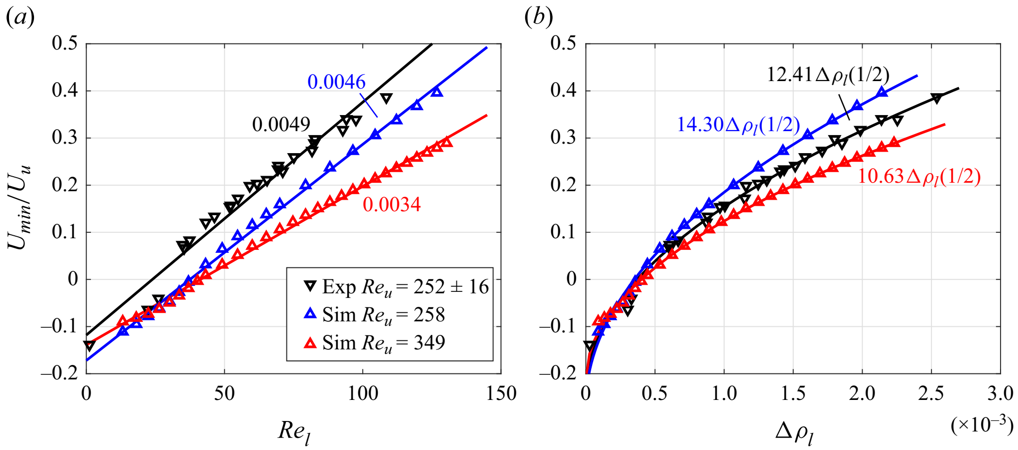

Figure 19. The variations of non-dimensional minimum velocity over (*a*) Re_l and (*b*) $\Delta\rho_l$. The Froude numbers are $Fr = 2.6 \pm 0.2$ for experiment, and $Fr = 2.6$ for simulation.

that the critical lower Reynolds numbers Re_l^* obtained from numerical simulations with different Re_u are very similar.

In our study, we adjust the fluid density to achieve various terminal Reynolds numbers, which are not known *a priori*. These terminal Reynolds numbers are correlated with density ratios through the velocity term, as we introduced at the end of § 1. Prior research has shown that the bouncing behaviour of particles is linked to the fluid density and density ratio (Doostmohammadi & Ardekani 2014*a*; Camassa *et al.* 2022). Thus it is necessary to investigate the relationship between the minimal velocity and the density ratio. Here, we define the density ratio as $\Delta\rho_l = (\rho_p - \rho_l)/\rho_l$. Substituting $U_l = \nu_l Re_l/D$ into (1.3), we can obtain an expression between the density ratio and the Reynolds number:

$$\Delta\rho_l = \frac{3C_{dl}\nu_l^2 Re_l^2}{4gD^3}, \tag{4.20}$$

where C_{dl} is the steady drag coefficient in the lower layer. Combining (4.19) and (4.20), we can obtain the following expression for the dependence of U_{min}/U_u on $\Delta\rho_l$:

$$\frac{U_{min}}{U_u} = c_1\sqrt{\frac{4gD^3}{3\nu_l^2 C_{dl}}}\,\Delta\rho_l^{1/2} + c_2. \tag{4.21}$$

We find that a power-law fitting in the form

$$\frac{U_{min}}{U_u} = c_3\,\Delta\rho_l^{1/2} + c_4 \tag{4.22}$$

is suitable for describing the dependence of U_{min}/U_u on $\Delta\rho_l$, as shown in figure 19(*b*) (recompiled data from figure 19*a*).

The trajectories and velocity profiles of particle P1 from experiment series 1 are presented in figure 20. Figure 20(*a*) demonstrates clearly that the bouncing behaviour substantially prolongs sedimentation time. While the particle enters the interface with the same velocity, slight variations in Re_l significantly affect its behaviour. For relatively large lower-layer Reynolds numbers, such as $Re_l = 59$, a minimum velocity is observed in figure 20(*b*), yet the particle continues to descend unidirectionally after passing through

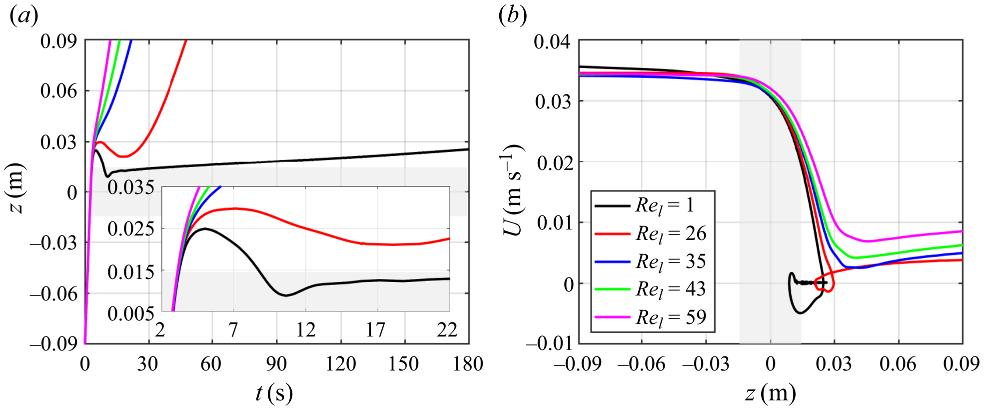

Figure 20. (*a*) Time trajectories of particles at five different lower Reynolds numbers. The non-monotonic trend indicates a bouncing behaviour. (*b*) The velocity profiles of particles at five different lower Reynolds numbers. The grey region refers to the density transition layer. Here, Fr and Re_u vary slightly, within $Fr =$ 2.4–2.5 and $Re_u = 236$–246.

the transition layer. We emphasise that all particles have a larger density than the fluid in the tank at all depths. As Re_l decreases and crosses a critical value, namely Re_l^*, as we have discussed previously, the particle reverses its direction of motion and ascends for a transient time scale (see figure 20(*a*) for $Re_l = 26$ and $Re_l = 1$). This bouncing phenomenon is characterised by a much deeper and negative minimum velocity, as shown in the depth versus velocity plot in figure 20(*b*). In this study, $Re_l = 1$ refers to an extreme case where the particle density ($\rho_p = 1123.69$ kg m^{-3}) is near the density of the bottom layer ($\rho_l = 1123.66$ kg m^{-3}). In this scenario, the particle experiences an extraordinarily long transient time scale to reach the terminal velocity of the bottom layer. As explained previously by Abaid *et al.* (2004), this long transient is due to the presence of a small boundary layer of upper fluid around the particle, which diffuses exceptionally slowly due to the long diffusion time of salt in water and the absence of strong turbulence diffusion in this low-speed flow state. This is further evidenced by our experimental results in figures 10(*p*–*t*), which clearly show that some light fluid remains on the particle surface after the bouncing.

It is worth noting that previous studies, such as Srdić-Mitrović *et al.* (1999), did not observe bouncing behaviour. They presented the time trajectories of particles obtained from a series of experiments (see their figure 9), reporting a noticeable decrease in velocity within the transition layer, but without finding reverse motion of the particle. This can possibly be explained by two factors. First, in their experiments, the upper fluid was a mixture of ethyl alcohol and water, which has different diffusion properties compared with our experiment. Thus the lighter upper fluid dragged by the particle could adjust to the surrounding fluid immediately, and weaken the deceleration of the particle. Second, and more importantly, their examined upper Reynolds numbers fall in the range $0.7 \leqslant Re_u \leq$ 23, which is much lower than in the current study. As we will discuss later, the upper Reynolds number is also one of the influencing factors for the occurrence of bouncing behaviour. In fact, the second explanation can be related to a deeper physical mechanism, namely the rear buoyant jet, which disappears when Re_u is low. As evidenced by the work of Yick *et al.* (2009), there was no sign of such a jet as $Re_u \sim 1$.

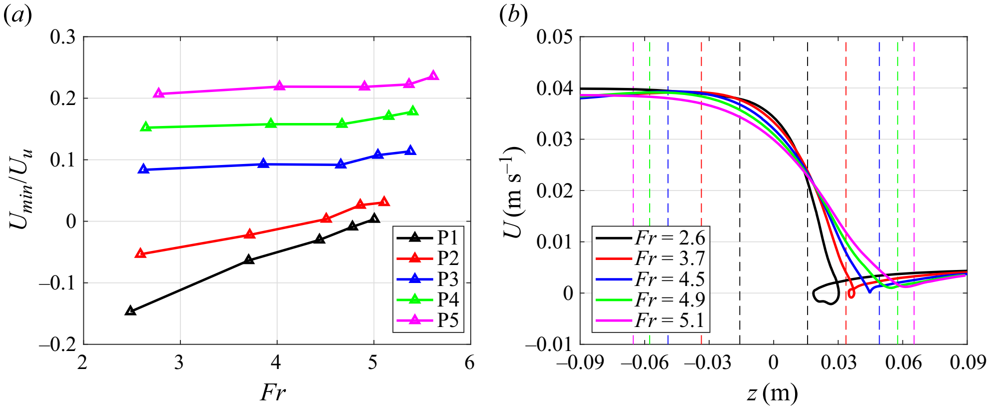

Figure 21. (a) The non-dimensional minimum velocity versus Froude number for five particles. The lower and upper Reynolds numbers are: P1, $Re_l = 12$, $Re_u = 286$; P2, $Re_l = 28$, $Re_u = 295$; P3, $Re_l = 44$, $Re_u = 303$; P4, $Re_l = 59$, $Re_u = 306$; P5, $Re_l = 77$, $Re_u = 317$. (b) The velocity profiles of particle P2 versus the vertical position at five Froude numbers. The vertical dashed lines indicate the bounds of the density transition layers.

4.4.2. *Froude number Fr*

We now examine the effects of Froude number. Specifically, we focus on experiment series 3 as presented in table 3. In this experiment, we keep the upper and lower layer fluid densities constant, and vary only the transition layer thickness by releasing particles into the same tank of fluid with a time interval of 24 h. This approach produces transition layer thickness variations in the range $L = 3.15$–13.06 cm, resulting in different Froude numbers.

Figure 21(a) shows the non-dimensional minimum velocities for different particles plotted over the Froude number. Note that the particle density increases from P1 to P5, which causes both the upper and lower Reynolds numbers to increase from P1 to P5. Overall, there is a nearly monotonic increase in the non-dimensional minimal velocity with increasing Froude number, i.e. as the transition layer becomes thicker. Furthermore, there is a noticeable increase in the minimum velocity when the particle density, or equivalently the Reynolds number, increases. However, for heavier particles such as P5, the role of the Froude number in increasing the minimum velocity is less significant (see P5 in figure 21a). In contrast, for lighter particles such as P1 and P2, the influence of the Froude number is considerable. For example, the behaviour of particle P2 changes from bouncing to unidirectional settling as the Froude number increases from $Fr = 2.6$ to $Fr = 5.1$. It is worth noting that for P2, the lower Reynolds number ($Re_l = 28$) is very close to the critical Reynolds number Re_l^*. We did not observe any bouncing phenomenon for P3, P4 and P5 in figure 21.

In figure 21(b), we present the velocity profiles of particle P2 at different Froude numbers. The Froude number significantly alters the evolving profile of particle settling velocity. We observe that the bouncing motion occurs after the particle leaves the transition layer (see $Fr = 2.6$ and 3.7 in figure 21b), while the minimum velocity is reached within the transition layer for those tests without bouncing (see $Fr = 4.5$, 4.9 and 5.1 in figure 21b). We also observed an interesting phenomenon: the particle restores to a higher settling velocity for the lower Froude number tests than that with high Froude numbers. This behaviour might be caused by the more pronounced diffusion induced by the jet flow. The jet flow can enhance the turbulence diffusion and diffuse the remaining upper layer fluid attached to the particle to its ambient lower layer fluid.

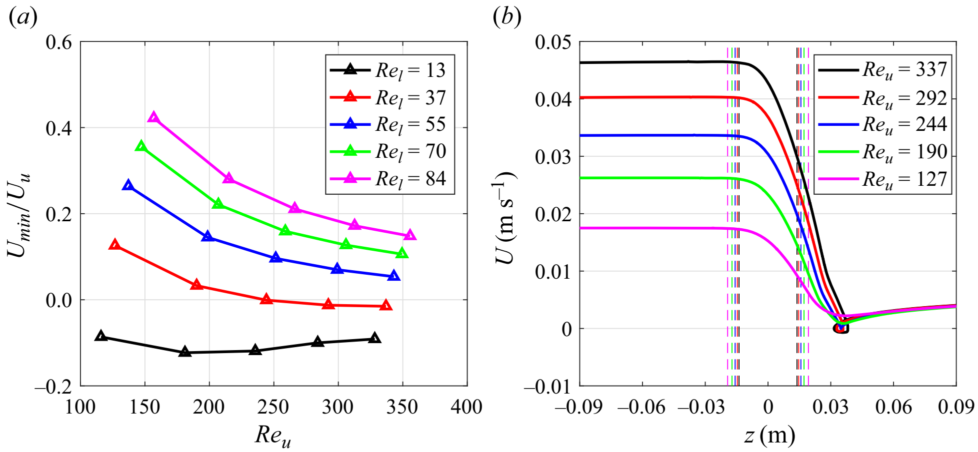

Figure 22. (*a*) The non-dimensional minimal velocity versus the upper Reynolds number at five lower Reynolds numbers, with $Fr = 2.6$. (*b*) The velocity versus vertical position corresponding to $Re_l = 37$ in (*a*).

4.4.3. *Upper Reynolds number Re_u*

We now investigate the effects of the upper Reynolds number (Re_u) using numerical simulations. In figure 22(*a*), we present the non-dimensional minimum velocity versus Re_u for five different values of Re_l at a fixed Froude number ($Fr = 2.6$). The trend is clear: the minimal velocity increases as the lower Reynolds number (Re_l) increases, while at a fixed Re_l, the minimal velocity decreases with increasing Re_u, except for $Re_l = 13$, where all minimal velocities are negative, indicating bouncing for all cases. We examine a special case, $Re_l = 37$, where the minimum velocity becomes negative as the upper Reynolds number increases to $Re_u = 292$. In figure 22(*b*), we plot the variations of settling velocity with depth for this special case. Despite the distinct differences in entering velocities of the particle among different tests, their minimal velocities are considerably similar. Furthermore, they reach minimal velocities at nearly the same depth. From figure 18, we understand that $Re_l = 37$ is near the critical Reynolds number for bouncing occurrence, making this special case highly sensitive to parameters such as the upper Reynolds number Re_u. As shown in figure 22(*b*), the particle moves unidirectionally for $Re_u = 127$, 190 and 244, while reversing its motion direction for $Re_u = 292$ and 337.

We stress that the upper Reynolds number Re_u plays a non-negligible role only when the bottom-layer Reynolds number Re_l is close to its critical value for bouncing. However, we note that the currently studied upper Reynolds numbers, in both experiments and numerical simulations, are kept at a certain order, $Re_u \sim O(100)$. A much lower Re_u, such as $\sim O(1)$, would give no sign of bouncing, as discussed in § 4.4.1.

4.4.4. *Identification of the bouncing regime in (Re_u, Fr) space*

Given that the bouncing behaviour is determined primarily by the lower Reynolds number Re_l, while the other two parameters, Re_u and Fr, can also play a role, as discussed in §§ 4.4.2 and 4.4.3, a better visualisation can be obtained by examining their combined effects. To illustrate, we present two maps in the parametric space of Re_u and Fr for two selected lower Reynolds numbers, $Re_l = 13$ and 37, with the contours representing the minimal velocities, in figure 23. It is evident from the figure that the bouncing phenomenon occurs in the higher Re_u and lower Fr regime, i.e. the upper left regions of the maps. A direct comparison between figures 23(*a*) and 23(*b*) indicates that the bouncing regime

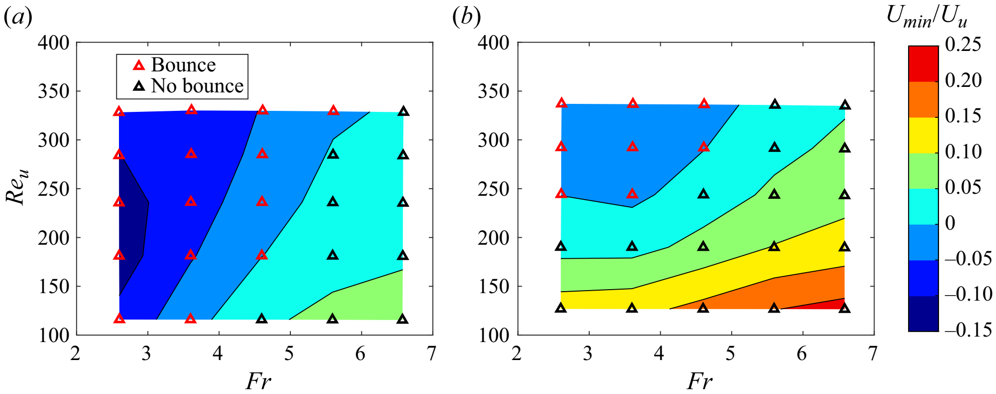

Figure 23. Maps of non-dimensional minimal velocities of the settling particle at (*a*) $Re_l = 13$, and (*b*) $Re_l = 37$.

	$Fr = 2.6$	$Fr = 3.6$	$Fr = 4.6$	$Fr = 5.6$	$Fr = 6.6$
$Re_u = 349$	41.0	46.2	44.5	25.5	—
$Re_u = 305$	39.6	43.7	39.4	14.4	—
$Re_u = 258$	37.5	40.0	31.9	—	—
$Re_u = 207$	34.6	34.2	21.8	—	—
$Re_u = 147$	28.9	24.3	—	—	—

Table 5. Critical lower Reynolds number Re_l^* in the (Re_u, Fr) space.

decreases for higher Re_l, further demonstrating that Re_l is the dominant parameter. When Re_l is low, the particles are more likely to bounce after passing through the transition layer.

By simulating in the same (Re_u, Fr) parametric space for different values of Re_l, we summarise the critical lower Reynolds numbers Re_l^* in table 5. At high Fr and low Re_u, the particle velocity varies smoothly from top to bottom, as shown in figures 21(*b*) and 22(*b*). In these cases, we cannot observe bouncing motion for the smallest density difference that we tested (corresponding to $Re_l = 13$). Therefore, we have not presented Re_l^* values for these cases. It can be seen from table 5 that Re_l^* varies from 14.4 to 46.2, depending on different combinations of Re_u and Fr. We should point out that the variations of Re_l^* with Fr at a fixed Re_u are not always monotonic, particularly when Re_u is high.

4.5. *Discussion on the strength of the buoyant jet*

To better understand the phenomenon of particle bouncing, it is important to examine the strength of the jet flow induced by the fluid. This can be achieved by quantifying the maximum jet velocity for each combination of Re_u and Fr, as shown in figure 24. In this figure, the lower Reynolds number is fixed at $Re_l = 37$. The maximum magnitude of jet velocity is identified at each test, which is scaled by the lower layer terminal velocity U_l. This non-dimensional jet velocity u_j/U_l is dependent primarily on Re_u, and its magnitude increases with increasing Re_u.

The jet velocity also exhibits a small dependency on Fr, decreasing in magnitude as Fr decreases. A higher magnitude of the jet leads to a greater drag force, resulting in a smaller U_{min} for the particle. The variation in jet strength provides a reasonable explanation for the

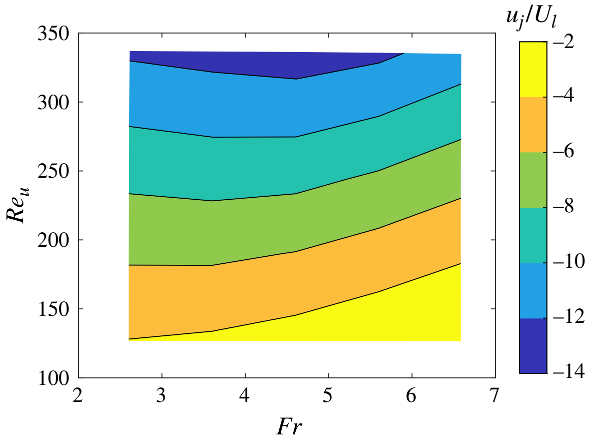

Figure 24. Jet velocities with maximum magnitudes in (Re_u, Fr) space at $Re_l = 37$. The negative value refers to an upward jet.

observed trends in U_{min} with respect to changes in Re_u and Fr (see figures 21(*b*) and 22(*b*)), that the decreasing of U_{min} with increasing Re_u or decreasing Fr is due to the increase in the upward jet velocity.

In previous research, Camassa *et al.* (2008) proposed a critical criterion for bouncing behaviour given by the equation

$$(\rho_p - \rho_l)V_p = (\rho_l - \rho_u)V_d, \tag{4.23}$$

where V_p represents the volume of the particle, and V_d represents the volume of the drift, which is the 'wake' formed at the rear of the particle as described in § 4.1. The satisfaction of (4.23) is based on three assumptions: (1) the bouncing motion occurs in the lower layer; (2) the unsteady forces F_a and F_h are negligible; (3) the stratification drag comes entirely from the buoyancy of the drift. These assumptions lead to a linear relationship between the densities of the fluid layers and the particle, as supported by experimental data and potential energy analysis in Camassa *et al.* (2022).

Equation (4.23) yields a linear correlation between the density triplet (ρ_u, ρ_l, ρ_p) and $\Delta\rho_l = (\rho_p - \rho_l)/\rho_l$, given by

$$\Delta\rho_l = -\frac{V_d}{V_p}\frac{\rho_u}{\rho_l} + \frac{V_d}{V_p}. \tag{4.24}$$

Figure 25(*a*) shows the variation of the critical density ratio $\Delta\rho_l^*$ over ρ_u/ρ_l at $Fr = 2.6$ and $Fr = 3.6$, corresponding to the critical cases presented in the first two columns of table 5. A quadratic fit is found to be more appropriate for the data than a linear regression.

We propose a possible explanation for the quadratic association between $\Delta\rho_l^*$ and ρ_u/ρ_l. As demonstrated in §§ 4.1 and 4.3.3, the jet dominates the stratification drag as the particle bounces. Assuming that the stratification drag is entirely due to the relative motion of the surrounding fluid with respect to the particle, the force balance can be expressed as

$$(\rho_p - \rho_l)gV_p = \tfrac{1}{2}C_d\rho_l U_r^2 S_p, \tag{4.25}$$

where U_r is the fluid velocity relative to the particle, and C_d is the steady drag coefficient. Equation (4.25) leads to a critical criterion for bouncing behaviour, given by $U_r \geqslant U_l$.

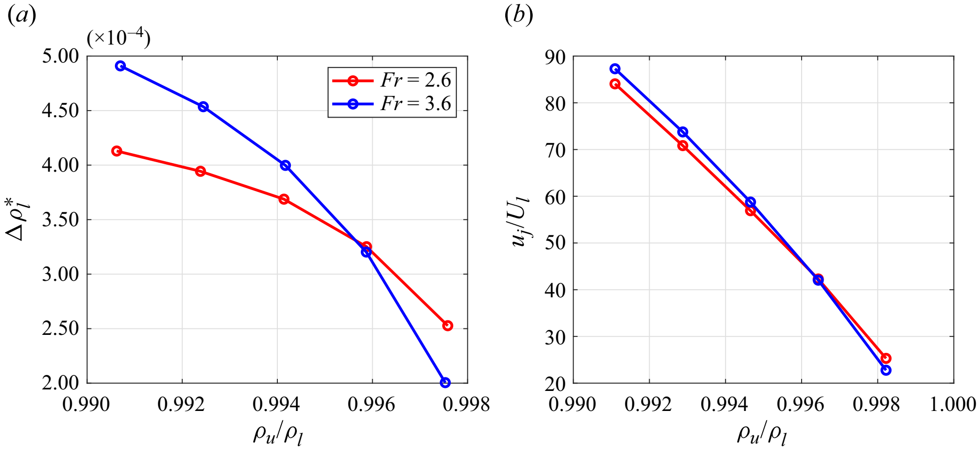

Figure 25. (*a*) The variation of critical density ratio $\Delta\rho_l^*$ over the density ratio ρ_u/ρ_l. (*b*) The variation of jet velocity over density ratio ρ_u/ρ_l at $Re_l = 13$.

This criterion yields a quadratic relationship between $\Delta\rho_l^*/\rho_l$ and U_r, given by

$$\Delta\rho_l = \frac{3C_d}{2gD} U_r^2. \tag{4.26}$$

The flow velocity U_r can be represented by the jet velocity u_j when the particle approaches zero velocity. In the studied parameter range, it was found that the jet velocity is linearly related to ρ_u/ρ_l when Fr is fixed, as shown in figure 25(*b*).

Based on the findings presented in (4.25), it can be inferred that there exists a quadratic correlation between $\Delta\rho_l^*$ and ρ_u/ρ_l. This observation highlights the significance of the jet velocity in determining the critical regime for the bouncing motion at the current parameter range.

5. Conclusions

In the present study, we conduct a comprehensive investigation into the physical mechanisms behind the bouncing behaviour, or reverse motion, of a spherical particle settling through a three-layer density-stratified fluid. Our research aims to reveal the forces acting on the particle and their correlation with the flow structure. We cover a wide range of parameters, including the lower-layer Reynolds number ($1 \leqslant Re_l \leqslant 125$), upper-layer Reynolds number ($115 \leqslant Re_u \leqslant 356$), Froude number ($2 \leqslant Fr \leqslant 7$) and Prandtl number ($Pr \approx 700$) for a salinity-stratified fluid.

First, we decompose the forces acting on the particle into different components, and correlate them with the flow structure. We observe four sequential stages of settling, including wake attachment, wake detachment, transient bouncing and final sedimentation. Two mechanisms are identified that contribute to drag enhancement, namely the buoyancy of the attached upper fluid and the force induced by the buoyancy jet flow, which arises from a specific flow structure. During the first two stages, the force component F_{sb} due to the attached upper fluid in the wake contributes mostly to the drag enhancement. However, at the third stage, most of the upper fluid has detached from the particle, and F_{sb} becomes less significant. Instead, the force component F_{sj} induced by the jet flow appears to be dominant. We confirm the existence of this jet flow through our experimental measurements, and we conclude that it is a necessary condition for the occurrence of bouncing motion.

Next, we investigate the influence of Re_l, Re_u and Fr. We monitor the minimal settling velocity of the particle, and a negative value indicates a bouncing motion. We find that the lower Reynolds number Re_l is the most significant determinant parameter. Our experiments reveal that bouncing motion occurs below a critical lower Reynolds number approximately $Re_l^* = 30$. In the numerical simulations, the highest value for this critical number is $Re_l^* = 46.2$, which is limited to the currently studied parametric ranges. Moreover, by quantifying the strength of the jet flow, we find a consistency between the maximum magnitude of jet velocity in the flow fields and the minimal settling velocity for the particle, plotted in the same (Re_u, Fr) space. This demonstrates the significance of jet flow on the particle's bouncing motion.

Although our study provides valuable insights into the bouncing behaviour of particles settling through a density-stratified fluid, it is clear that further research is needed. For instance, it would be interesting to consider a cluster of particles, where interactions between particles can lead to more complex and intriguing settling behaviours. Also, particles with irregular shapes can be investigated, which would more closely resemble real-world scenarios, such as the aggregation of marine snow.

Funding. This research has been supported by the National Natural Science Foundation of China (grant no. 92252102). S.W. gratefully acknowledges the hospitality of the Department of Applied Mathematics and Theoretical Physics, University of Cambridge.

Declaration of interests. The authors report no conflict of interest.

Author ORCIDs.
Jian Deng https://orcid.org/0000-0001-6335-498X;
C.P. Caulfield https://orcid.org/0000-0002-3170-9480.

REFERENCES

ABAID, N., ADALSTEINSSON, D., AGYAPONG, A. & MCLAUGHLIN, R.M. 2004 An internal splash: levitation of falling spheres in stratified fluids. *Phys. Fluids* **16** (5), 1567–1580.

AHMERKAMP, S., LIU, B., KINDLER, K., MAERZ, J., STOCKER, R., KUYPERS, M.M.M. & KHALILI, A. 2022 Settling of highly porous and impermeable particles in linear stratification: implications for marine aggregates. *J. Fluid Mech.* **931**, A9.

ARDEKANI, A.M. & STOCKER, R. 2010 Stratlets: low Reynolds number point-force solutions in a stratified fluid. *Phys. Rev. Lett.* **105** (8), 084502.

BAYAREH, M., DOOSTMOHAMMADI, A., DABIRI, S. & ARDEKANI, A.M. 2013 On the rising motion of a drop in stratified fluids. *Phys. Fluids* **25** (10), 023029.

BLANCHETTE, F. & SHAPIRO, A.M. 2012 Drops settling in sharp stratification with and without Marangoni effects. *Phys. Fluids* **24** (4), 042104.

CAMASSA, R., DING, L., MCLAUGHLIN, R.M., OVERMAN, R., PARKER, R. & VAIDYA, A. 2022 Critical density triplets for the arrestment of a sphere falling in a sharply stratified fluid. In *Recent Advances in Mechanics and Fluid–Structure Interaction with Applications: The Bong Jae Chung Memorial Volume* (ed. F. Carapau & A. Vaidya), pp. 69–91. Springer.

CAMASSA, R., FALCON, C., LIN, J., MCLAUGHLIN, R.M. & MYKINS, N. 2010 A first-principle predictive theory for a sphere falling through sharply stratified fluid at low Reynolds number. *J. Fluid Mech.* **664**, 436–465.

CAMASSA, R., FALCON, C., LIN, J., MCLAUGHLIN, R.M. & PARKER, R. 2009 Prolonged residence times for particles settling through stratified miscible fluids in the Stokes regime. *Phys. Fluids* **21** (3), 031702.

CAMASSA, R., MCLAUGHLIN, R.M., MOORE, M.N.J. & VAIDYA, A. 2008 Brachistochrones in potential flow and the connection to Darwin's theorem. *Phys. Lett.* A **372** (45), 6742–6749.

DENG, J. & CAULFIELD, C.P. 2016 Dependence on aspect ratio of symmetry breaking for oscillating foils: implications for flapping flight. *J. Fluid Mech.* **787**, 16–49.

DIERCKS, A., ZIERVOGEL, K., SIBERT, R., JOYE, S.B., ASPER, V. & MONTOYA, J.P. 2019 Vertical marine snow distribution in the stratified, hypersaline, and anoxic Orca Basin (Gulf of Mexico). *Elementa: Sci. Anthropocene* **7**, 10.

DOOSTMOHAMMADI, A. & ARDEKANI, A.M. 2014*a* Reorientation of elongated particles at density interfaces. *Phys. Rev.* E **90** (3), 033013.

DOOSTMOHAMMADI, A., DABIRI, S. & ARDEKANI, A.M. 2014*b* A numerical study of the dynamics of a particle settling at moderate Reynolds numbers in a linearly stratified fluid. *J. Fluid Mech.* **750**, 5–32.

ECONOMIDOU, M. & HUNT, G.R. 2009 Density stratified environments: the double-tank method. *Exp. Fluids* **46**, 453–466.

EPPS, B.P. 2010 An impulse framework for hydrodynamic force analysis: fish propulsion, water entry of spheres, and marine propellers. PhD thesis, Massachusetts Institute of Technology.

FERZIGER, J.H. & PERIĆ, M. 2002 *Computational Methods for Fluid Dynamics*. Springer.

HANAZAKI, H., KASHIMOTO, K. & OKAMURA, T. 2009 Jets generated by a sphere moving vertically in a stratified fluid. *J. Fluid Mech.* **638**, 173.

HIGGINSON, R.C., DALZIEL, S.B. & LINDEN, P.F. 2003 The drag on a vertically moving grid of bars in a linearly stratified fluid. *Exp. Fluids* **34** (6), 678–686.

JASAK, H. 2009 Dynamic mesh handling in OpenFOAM. In *47th AIAA Aerospace Sciences Meeting Including the New Horizons Forum and Aerospace Exposition*, Orlando, FL, USA. *AIAA Paper* 2009-341. AIAA.

MAGNAUDET, J. & MERCIER, M.J. 2020 Particles, drops, and bubbles moving across sharp interfaces and stratified layers. *Annu. Rev. Fluid Mech.* **52**, 61–91.

MANDEL, T.L., WALDROP, L., THEILLARD, M., KLECKNER, D. & KHATRI, S. 2020 Retention of rising droplets in density stratification. *Phys. Rev. Fluids* **5** (12), 124803.

MORDANT, N. & PINTON, J.F. 2000 Velocity measurement of a settling sphere. *Eur. Phys. J.* B **18** (2), 343–352.

MORE, R.V. & ARDEKANI, A.M. 2023 Motion in stratified fluids. *Annu. Rev. Fluid Mech.* **55**, 157–192.

MORE, R.V., ARDEKANI, M.N., BRANDT, L. & ARDEKANI, A.M. 2021 Orientation instability of settling spheroids in a linearly density-stratified fluid. *J. Fluid Mech.* **929**, A7.

MROKOWSKA, M.M. 2018 Stratification-induced reorientation of disk settling through ambient density transition. *Sci. Rep.* **8** (1), 1–12.

MROKOWSKA, M.M. 2020 Influence of pycnocline on settling behaviour of non-spherical particle and wake evolution. *Sci. Rep.* **10** (1), 20595.

OKINO, S., AKIYAMA, S. & HANAZAKI, H. 2017 Velocity distribution around a sphere descending in a linearly stratified fluid. *J. Fluid Mech.* **826**, 759–780.

OKINO, S., AKIYAMA, S., TAKAGI, K. & HANAZAKI, H. 2021 Density distribution in the flow past a sphere descending in a salt-stratified fluid. *J. Fluid Mech.* **927**, A15.

PRAIRIE, J.C. & WHITE, B.L. 2017 A model for thin layer formation by delayed particle settling at sharp density gradients. *Cont. Shelf Res.* **133**, 37–46.

SCHLICHTING, H. & KLAUS, J. 2003 *Boundary-Layer Theory*. Springer Science & Business Media.

SHARQAWY, M.H., Lienhard, J.H. & Zubair, S.M. 2010 Thermophysical properties of seawater: a review of existing correlations and data. *Desalination Water Treatment* **16** (1–3), 354–380.

SRDIĆ-MITROVIĆ, A.N., MOHAMED, N.A. & FERNANDO, H.J.S. 1999 Gravitational settling of particles through density interfaces. *J. Fluid Mech.* **381**, 175–198.

TORRES, C.R., HANAZAKI, H., OCHOA, J., CASTILLO, J. & VAN WOERT, M. 2000 Flow past a sphere moving vertically in a stratified diffusive fluid. *J. Fluid Mech.* **417**, 211–236.

TRUSCOTT, T.T., EPPS, B.P. & TECHET, A.H. 2012 Unsteady forces on spheres during free-surface water entry. *J. Fluid Mech.* **704**, 173–210.

VERSO, L., VAN REEUWIJK, M. & LIBERZON, A. 2019 Transient stratification force on particles crossing a density interface. *Intl J. Multiphase Flow* **121**, 103109.

WANG, S., WANG, J. & DENG, J. 2023 Effect of layer thickness for the bounce of a particle settling through a density transition layer. *Phys. Rev.* E **108** (6), 065108.

WHITE, F.M. & MAJDALANI, J. 2006 *Viscous Fluid Flow*. McGraw-Hill.

YICK, K.Y., TORRES, C.R., PEACOCK, T. & STOCKER, R. 2009 Enhanced drag of a sphere settling in a stratified fluid at small Reynolds numbers. *J. Fluid Mech.* **632**, 49–68.

ZHANG, J., MERCIER, M.J. & MAGNAUDET, J. 2019 Core mechanisms of drag enhancement on bodies settling in a stratified fluid. *J. Fluid Mech.* **875**, 622–656.